Measurement of Single Spin Asymmetry and Cross Section for Direct Photon Production in pp Collisions at 200 GeV/c

AUTHOR(S):

Saito, Naohito

CITATION:

Saito, Naohito. Measurement of Single Spin Asymmetry and Cross Section for Direct Photon Production in pp Collisions at 200 GeV/c. Memoirs of the Faculty of Science, Kyoto University. Series of physics, astrophysics, geophysics and chemistry 1996, 39(3): 431-484

ISSUE DATE:

1996-03

URL:

http://hdl.handle.net/2433/257639

Memoirs of the Faculty of Science, Kyoto University, Series of Physics, Astrophysics, Geophysics and Chemistry, Vol. XXXIX, No. 3, Article 4, 1996

Measurement of Single Spin Asymmetry and Cross Section for Direct Photon Production in *pp* Collisions at 200 GeV/c

By

Naohito SAITO[1]

Department of Physics, Faculty of Science, Kyoto University, Kyoto 606-01, Japan

(Received November 22, 1995)

abstract

The single transverse-spin asymmetry for inclusive direct photon production has been measured using a polarized proton beam of 200 GeV/c upon an unpolarized proton target in $-0.15 < x_F < 0.15$ and $2.5 < p_T < 3.1$ GeV/c at Fermilab. The data on the cross section for $pp \rightarrow \gamma X$ in $2.5 < p_T < 3.8$ GeV/c have also been provided. The measurement has been done using lead glass calorimeters and photon detectors which surrounded the fiducial area of the calorimeters. Those detectors have been located at 90° in the center of mass frame. Background rejection has been done using the surrounding photon detectors. The cross section obtained is consistent with the results of previous measurements, if we assume the cross section is proportional to the atomic number. The comparisons of the cross section with theoretical calculations have been made. The single transverse-spin asymmetry, A_N, for the direct photon production is consistent with zero within the experimental uncertainty.

1 Introduction

Since the late 1960's, the structure of nucleon has been investigated in deep-inelastic scattering of lepton from the nucleon [1, 2]. Such studies have led to a successful description of the internal structure of hadrons by a quark-parton model [3]. The set of the input data for the model has been extended to include the Drell-Yan production of lepton pairs, direct-photon production, heavy flavor production, and weak boson productions [4]. The study of the hadron structure plays important roles in particle physics. One of them is to provide a precision test of quantum chromodynamics (QCD). The other is to convert the luminosity of hadron beam to the luminosities of quarks and gluons. The importance of the former one has been demonstrated in the early stage of the study by the discovery of the asymptotic freedom, which is the basic aspect of QCD. The importance of the latter can be easily understood if we consider high-energy hadron collisions. Without the knowledge of the quark and gluon luminosities, it is hard to relate the physical observables to the fundamental parton subprocesses.

For a concrete view on the relation between the structure functions and the

[1] Present address : Radiation Laboratory, RIKEN, Wako-shi, Saitama, 351-01, Japan

physical observables, let us think of the invariant cross section for inclusive production of particle C in the collision of hadrons A and B, $A+B \rightarrow C+X$. The reaction is shown schematically in Figure 1. The cross section for the reaction is expressed at the leading order as

$$E\frac{d^3\sigma}{dp^3} \sim \sum_{abcd} G_{a/A}(x_a) \otimes G_{b/B}(x_b) \otimes \frac{d\sigma}{d\hat{t}}(ab \rightarrow cd) \otimes D_{C/c}(z_c). \quad (1)$$

Here x_i ($i = a$, b, c, and d) represents the momentum fraction carried by the parton i. The probability of finding a parton a in the hadron A with a momentum fraction lying between x_a and $x_a + dx_a$ is denoted by the structure function $G_{a/A}(x_a)$. The probability of obtaining a particle C with a momentum fraction between z_c and $z_c + dz_c$ from a parton c is denoted by the fragmentation function $D_{C/c}(z_c)$. The cross section for the parton reaction $ab \rightarrow cd$, is denoted by $\frac{d\sigma}{d\hat{t}}(ab \rightarrow cd)$. The summation includes all the possible subprocesses.

Among experimental studies of the hadron structure, the direct-photon production provides the gluon distribution at the leading order. The term "direct photon" means the photon originating from an interaction of partons unlike the photon from the production of the hadron that subsequently decays electromagnetically. The production of photons with high transverse momentum, p_T, is dominated by the gluon "Compton" subprocess ($qg \rightarrow \gamma q$) and the annihilation subprocess ($q\bar{q} \rightarrow \gamma g$) (Figure 2). In particular, the gluon "Compton" subprocess dominates the direct-photon production in pp collisions. If we replace the final photon in the gluon "Compton" subprocess by gluon, we have 2-jet productions ($qg \rightarrow qg$). One of the advantages of the direct-photon production is that the direct photon is produced mostly via single subprocess, while a variety of subprocess contribute to the 2-jet production. Another advantage is that the 4-momentum of photon is generally determined with better resolution than that of a jet. Therefore the data of cross sections for direct-photon production have been used for obtaining the gluon distribution inside the proton [5, 6, 7].

Listed in Table 1 are the experiments of direct-photon production in pp collisions at high-p_T. The data are provided in the wide range of the center of mass energy, $19.4 \leq \sqrt{s} \leq 63.0$ GeV. There is, however, no data on pure pp collisions at $\sqrt{s} =$

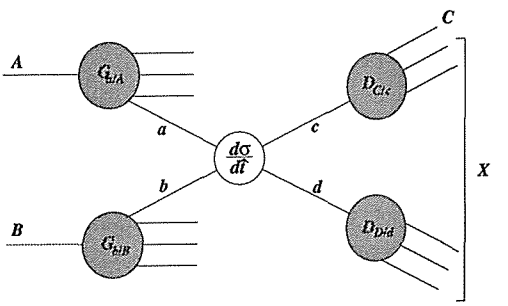

Fig. 1. Schematic representation of the high-p_T reaction factorized into parton distribution functions (G), parton fragmentation functions (D), and a hard-scattering subprocess, $d\sigma/d\hat{t}$ ($ab \rightarrow cd$).

Table 1. Experiments on direct-photon production in pp collisions. The experiments marked by " ★ " used nuclear target instead of proton target.

Collaboration	$\sqrt{s}$(GeV)	$p_T^{\max}$(GeV/c)	Reference
UA-6(CERN)	24.3	6.1	[8]
E7060FNAL)★	30.6	8.0	[9]
R110(CERN)	63.0	10.0	[10]
R807(CERN)	63.0	11.0	[11]
WA70(CERN)	22.9	7.0	[12]
NA24(CERN)	23.7	6.0	[13]
NA3(CERN)★	19.4	5.0	[14]
E629(FNAL)★	19.4	4.5	[15]

19.4 GeV. The high-p_T reaction in pA collisions may be influenced by a nuclear dependence of structure functions ("EMC effect") [16 – 19] and by "higher-twist" contributions [20], which are suppressed by a power of $(\frac{1}{\sqrt{Q^2}})$ with respect to the leading terms. To reject such unknown effects, the pure pp data is desirable in this energy region [21, 22].

The investigation of the structure of nucleon has been extended to include the freedom of spin with works of the SLAC-Yale collaborationin the early 1970's [23 – 25]. The surprising result published in 1987 by the European Muon Collaboration (EMC) [26] has stimulated the reconsideration of spin effects in inelastic processes. The measurement of $g_1^p(x)$ using the polarized-muon beam on the polarized target by the EMC has been interpreted as a direct measure of the fraction of the proton spin carried by quarks. The result, $12.0 \pm 9.4 \pm 13.8\%$, was significantly smaller than the value previously predicted, $60 \pm 12\%$ [27, 28]. The deviation of the theoretical prediction from the experimental data has been reduced by further studies [29], but their data has motivated both experimental and theoretical work much in the field of the spin structure of nucleon.

In this context, the higher-twist effect has drawn much attention especially in relevance to the single transverse-spin asymmetry, A_N. Here the parameter, A_N, represents "*left-right asymmetry*" of the cross sections with the vertically-polarized proton beam as

$$A_N = \frac{\sigma_L - \sigma_R}{\sigma_L + \sigma_R}, \tag{2}$$

where the cross section for the particle production in left (right) side is denoted by σ_L (σ_R). It has been widely believed that the asymmetry A_N is essentially zero in high-energy hadron reactions. It has, however, been pointed out that the A_N in high-energy reactions may not be zero due to higher-twist effects [30, 31].

A simple generalization of the QCD-factorization in Equation (1) suggests that the single spin asymmetry can be qualitatively described as

$$A_N \sim \sum_{abcd} \Delta_T G_{a/A}(x_a) \otimes G_{b/B}(x_b) \otimes \hat{a}_N(ab \to cd) \otimes D_{C/c}(z_c). \tag{3}$$

Here $\Delta_T G_{a/A} = G_{a\uparrow/A\uparrow} - G_{a\downarrow/A\uparrow}$ is the difference between the number density of parton a with spin "up" in the spin "up" hadron A and the number density of parton a with spin "down" in the spin "up" hadron A. The $\hat{a}_N$ $(ab \to cd)$ stands for the single transverse-spin asymmetry in the subprocess, $ab \to cd$. Any of $\Delta_T G_{a/A}(x_a)$, $\hat{a}_N$, and $D_{C/c}(z_c)$ is responsible for the A_N.

Qiu and Sterman [32] have predicted the asymmetry A_N for direct-photon production. According to them, A_N for direct-photon production in pp collisions is due to the quark-gluon correlation function, $T(x, s_T)$, which is the twist-3 matrix element. Here s_T indicates the transverse spin of the nucleon, which can be either of "up" or "down". The twist-3 matrix element is a part of $\Delta_T G_{a/A}(x_a)$. They have made models of the twist-3 matrix element, $T(x, s_T)$, shown as

$$T_I(x, s_T) \approx 0.2 F_2(x)/x \quad \text{(GeV)} \quad \text{(model I)}, \tag{4}$$

$$T_{II}(x, s_T) \approx 0.2 F_2(x) \quad \text{(GeV)} \quad \text{(model II)}. \tag{5}$$

Using these matrix elements, they have predicted a large asymmetry A_N, that is 3 to 10% at $x_F = 0$, as shown in Figure 3. They have pointed out that the asymmetry at positive x_F in pp collisions with a polarized proton beam and an unpolarized target is mainly attributed to the quark-gluon correlation. Ji [33] has suggested that the pure gluon-correlation contributes to the asymmetry at large negative x_F value. On the other hand, Schäfer *et al.* [34] have proposed alternative choice of the twist-3 matrix

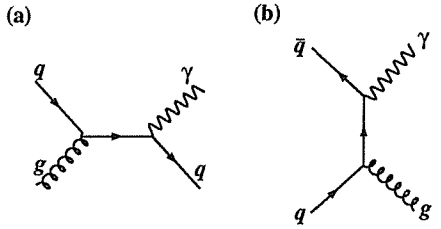

Fig. 2. Diagrams of subprocesses contributing to the direct-photon production at the leading order, (a) gluon "Compton" and (b) annihilation subprocesses.

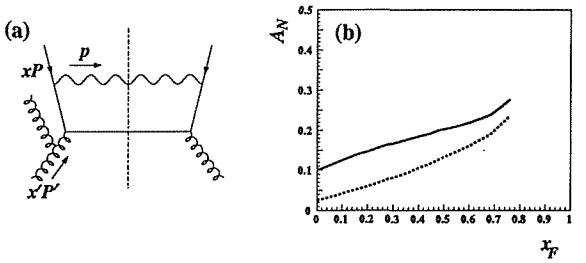

Fig. 3. (a) An example of the diagram contributing to the single transverse-spin asymmetry for direct-photon production.(b) Asymmetry A_N as a function of x_F at $\sqrt{s} = 30$ GeV and $p_T = 4$ GeV/c. The solid curve is computed using the twist-3 matrix element in Equation (4), the dotted curve using the one in Equation (5).

element, and have predicted smaller asymmetry. Efremov and Teryaev [35] have claimed completely zero asymmetry at $x_F = 0$. It should be noted that in any model the sign of the asymmetry is not specified and must be determined experimentally[2]. Consequently, experimental data are indispensable to elucidate the spin structure of nucleon at the twist-3 level.

In spite of the importance of the direct-photon production process, any spin parameter of the process has never been measured. This is mainly due to the lack of sufficiently high-energy polarized-proton beam and/or pure polarized-proton target. We have overcome this problem with successful commissioning of the polarized proton beam of 200 GeV/c. The source of the polarized proton is in parity-violating decay of the Λ hyperon.

Even with the high-energy polarized-proton beam, there is further experimental difficulty in discriminating the direct photon against photons from radiative decay of neutral mesons such as $\pi^0 \to \gamma\gamma$ and $\eta \to \gamma\gamma$. The rate for the direct-photon production is greatly suppressed comparing to that for the jet production, because the leading contribution to the direct-photon production is order of $\alpha\alpha_s$, while the jet production is proportional to α_s^2. A number of background-rejection methods have been employed in previous measurements.

In the *reconstruction* method, the photon which forms an invariant mass of π^0 or η with another photon is rejected. Usually this method requires a calorimeter with large fiducial area. Smaller coverage will result in a large amount of background originated from unreconstructed neutral mesons. Remaining background must be subtracted statistically. Therefore, the precise measurement of π^0 and η is required. Furthermore, the *reconstruction* method is not so effective especially for the high-p_T π^0, since the opening angle of two photons from the decay becomes narrow. The distance, r, between two photons from the π^0 decay at the position of the surface of the calorimeter is expressed as

$$r \sim \frac{2M_{\pi^0}L}{\gamma p_T}. \tag{6}$$

Here M_{π^0} represents the mass of π^0 and L indicates the distance from the decay point to the surface of the calorimeter. The γ denotes the Lorentz factor for the transformation from the laboratory frame to the center-of-mass system, and p_T stands for the transverse momentum of the π^0 meson. The two photons from π^0 decays will merge into one shower due to the finite resolution of the detector, and will fake direct-photon events. Hence, high capability to separate two showers is indispensable.

The *isolation* method requires photon candidates not to be accompanied by other particles inside a cone of a certain radius $R\ (= \sqrt{\Delta\eta^2 + \Delta\phi^2})$ centered on the photon direction (*isolation cone*), where η and ϕ represents the pseudo-rapidity, and the azimuthal angle, respectively. The term "not to be accompanied" means that the amount of additional energy inside the cone is less than a certain fraction of the photon energy or less than certain energy. The application of the *isolation cut*

[2] Schäfer *et al.* have given some evidence for their expectation of negative asymmetry, but have not come to the definite conclusion.

discriminates strongly against π^0 events, since a π^0 is usually accompanied by additional particles from fragmentation of jet. Direct photons from leading order processes are unaffected by this cut, since the photon is isolated.

We have employed both of these techniques to overcome the experimental difficulties. The π^0 mesons and η mesons, which are the dominant background sources for direct photons, have been reconstructed using a lead-glass calorimeter which covers $| x_F | \leq 0.1$. Fine granuality of the lead-glass calorimeter allows us good efficiency of the two-shower separation and reduces the background from π^0 and η events. The measured yields of these mesons provide the basis of the background evaluation.

For further discrimination of direct-photon events from the background, one of the possible ways is the *isolation cut* using the calorimeter itself. In the case of our experiment, however, the ratio of the signal to noise is about 1:5 according to a Monte Carlo simulation. We have extended the *isolation cone* by installing the photon detector which surrounds the fiducial area of the calorimeter like a "picture frame" to reduce the background contribution. The photon detector has dual roles; one is to reject π^0 and η events by detecting one photon from their decays and the other is to suppress the background by requiring an *isolation* from other photon sources. The detector is not necessarily sensitive to the energy of photon for the requirement of *isolation*. Hence the installed photon detector consists of three plastic scintillators and two lead-plate converters inserted inbetween. According to a Monte Carlo simulation, the ratio of the signal to noise is expected to be improved to 1:1 by the photon detector.

Section 2 describes the experimental procedure with emphasis put on the design and the operation of the polarized-proton beam line, the lead-glass calorimeter, and the surrounding photon detector. In Section 3, the reconstruction of 4-momenta of photons is presented. Reconstructions of tracks of charged particlesand event vertices are also described. The details of the analysis for the π^0 production are discussed in Section 4. Section 5 describes the analysis procedure to extract the cross section and asymmetry A_N for the direct-photon production. In Section 6, the results on the cross section for the direct-photon production, and on the asymmetry for the direct-photon production are presented and discussed. The conclusion is in Section 7.

2 Experiment

This section describes the designs, the construction, and the performance of the experimental apparatus.

The experiment 704 has been performed from the end of January to the middle of August in 1990 at the Meson Area at Fermilab. The polarized proton/antiproton beam originated from the parity violating decay of the $\Lambda / \bar{\Lambda}$. The polarization of the beam was tagged at the intermediate focal point utilizing the correlation between the polarization and the beam position. The spin was rotated to the demanded direction using spin-rotation magnets. The proton/antiproton beam with the demanded spin direction hit the experimental target, which was the liquid hydrogen target. The

photons and electrons generated in the reaction were detected using two sets of lead-glass calorimeters. The tracks of charged particles were detected using a set of MWPC's. A set of photon detectors was installed to reject the background mentioned in the previous section.

2.1 Beam Line

2.1.1 Polarized-Proton Beam

A polarized proton/anti-proton beam line of 200 GeV/*c* was constructed in the Meson Area of Fermilab [37]. The polarized proton/antiproton originated from the parity violating decay of $\Lambda/\bar{\Lambda}$.

The proton beam of 800 GeV/*c* from the TEVATRON was divided into the MC beam line and the MP beam line, which we used. The beam profile of the MP beam line was monitored with four segmented-wire ion chambers (SWIC). A secondary-emission monitor (SEM) was used for measuring the primary-beam intensity just upstream of the production target (see Figure 4). A typical intensity during our measurement was 2×10^{12} protons per spill (= 20 sec).

The beam line consisted of the Λ production/decay area, the beam tagging area, and the spin-rotation areaas shown in Figure 5. The production target was a

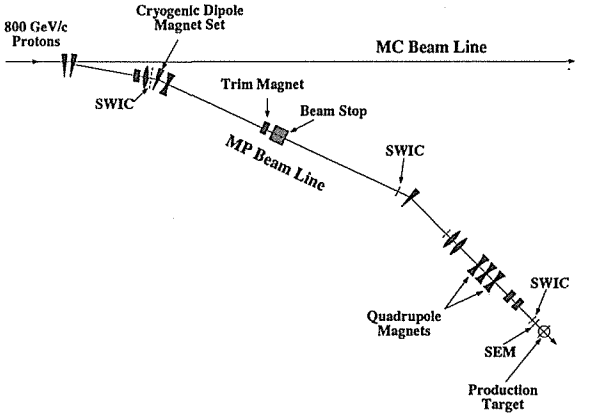

Fig. 4. Diagram of the primary beam line. Shown are the split from the MC beam line, the two sets of cryogenic bending magnets, beam-line detectors (SWIC and SEM) and the production target.

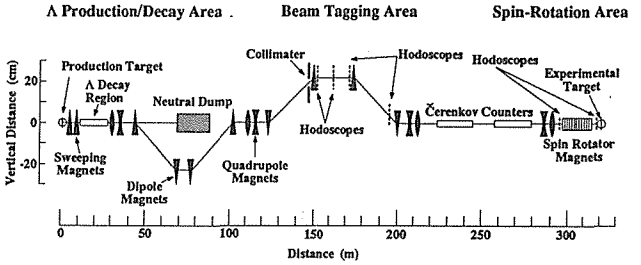

Fig. 5. Beam-line elements downstream of the production target.

beryllium wire. The target had a width of 1.5 mm, a height of 5.0 mm, and was 30.0 cm long. The charged particles produced in the target were deflected out by sweeping magnets located downstream of the target. In the decay region of about 20 m, approximately a half of Λ hyperons decayed in the energy region of interest. Neutral particles were absorbed in the neutral dump.

In the rest frame of the Λ, the decay $\Lambda \rightarrow p\pi^-$ occurs isotropically and the polarization of the decay proton is 64% with the spin direction along the proton momentum. The spin direction is not changed under the Lorentz transformation from the rest frame to the laboratory frame (see Figure 6 (a)). For Λ's which decay at a fixed distance from the target, the trajectories of the decay protons with the same transverse spin component are traced back to the same point on the plane which is normal to the beam axis at the production point regardless of the direction of Λ momentum in the laboratory frame as shown in Figure 6 (b). The image of the traced-back beam positions in the plane is called the "virtual source" of polarized protons.

The momentum of the beam particle was selected by the dipole magnets downstream of the decay region. The momentum bite was about $\pm 30\%$ after this selection. The momentum of the beam particle was further selected with the collimator located just upstream of the beam tagging area. The momentum bite of transmitted particle was $\pm 9\%$.

2.1.2 Beam Tagging System

The beam tagging system was constructed near the intermediate focal point, that was 150-m downstream of the production target. The tagging system consisted of tagging hodoscopes. The location of the hodoscopes are schematically shown in Figure 7. The dimensions and the segmentation are listed in Table 2. The polarization hodoscopes, POL1, POL2, and POL3 were segmented in the horizontal direction (x), and the momentum hodoscopes, MOM1, MOM2 and MOM3 were in the vertical direction (y). All the hodoscopes consisted of 14 scintillators and one third of the width was overlapped each other as shown in Figure 8.

The horizontal beam-trajectory was measured using two hodoscopes POL1 and POL3. The third hodoscope POL2 located at the intermediate focal point was used for redundancy check. The image of the "virtual source" was obtained here and used for tagging the polarization. Figure 9 shows the correlation between the average

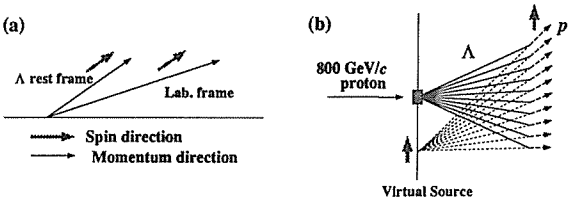

Fig. 6. (a) Spin and momentum directions of the proton from the Λ-decay at the production point of Λ hyperons. The spin direction is not changed by the Lorentz boost from the restframe of Λ to the laboratory frame. The idea of "virtual source" of polarized proton beam is shown in (b). See the text for details.

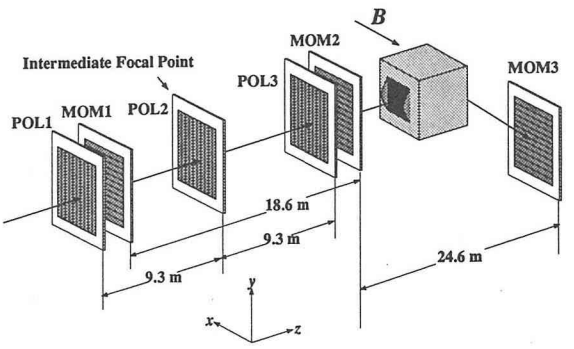

Fig. 7. Layout of tagging hodoscopes at the intermediate focal point. Polarization hodoscopes are segmented in x-direction and momentum hodoscopes are segmented in y-direction. See Table 2 for the parameters of each hodoscopes.

Table 2. Parameters of tagging hodoscopes.

hodoscope	dimensions (mm)				segmentation	
	width	length	thickness	direction	size(mm)	number
POL1,2,3	6.0	115	3.0	x	2.0	27
MOM1,2,3	10.0	120	3.0	y	3.33	27

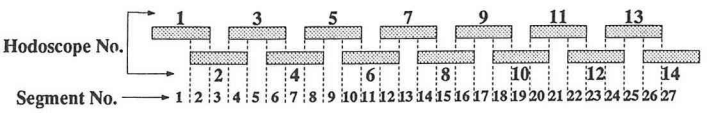

Fig. 8. Configuration of tagging hodoscopes. One third of the width of the scintillator was overlapped each other.

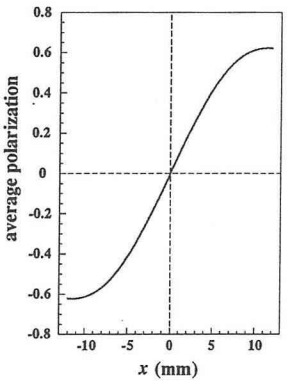

Fig. 9. x-position dependence of beam polarization.

particle polarization and the horizontal position at the intermediate focal point, which is the result of the simulation of the beam line. The measured horizontal position of each beam particle was translated to a polarization according to the correlation shown in Figure 9. The ratio of the number of the beam particles tagged by the polarization hodoscopes in each polarization bin of 10% interval to the total number of the beam particles is plotted in Figure 10 (a). The accuracy of the alignment of the hodoscopes was 0.5 mm. Correspondingly, the accuracy of polarization measured with this method was $\pm$ 1.9%. The phase space of the beam was divided with respect to the polarization, P_B, into three parts, $P_B < -0.35$, $|P_B| < 0.35$, and $P_B > 0.35$. The average polarization for those three parts were $-$ 46%, 0%, and + 46%, respectively. We refer to these three parts as positively-polarized, unpolarized, and negatively-polarized part of the beam. A typical intensity of the beam was 2×10^7 protons per spill (= 20 sec). About a half of the beam was substantially polarized.

The average polarization of the proton beam was measured prior to the present experiment by two independent methods; one is the Primakoff polarimeter method and the other is the Coulomb-Nuclear-Interference (CNI) method. The polarization was measured also during the present experiment by the CNI method.

The Primakoff polarimeter method determines the polarization of the proton beam by measuring the asymmetry for the process,

$$p+Z \rightarrow \Delta/N^* + Z \rightarrow p+\pi^0+Z, \tag{7}$$

where Z is the high-Z nucleus and the Δ and N^* are the resonant intermediate states. Here the fundamental process is considered as

$$p+\gamma^* \rightarrow \Delta/N^* \rightarrow p+\pi^0. \tag{8}$$

The absolute polarization of the proton beam was obtained by comparing the measured asymmetry [38] with the asymmetry of the photo-production process measured at low energy ($\sim$ 700 MeV) [40].

The CNI method determines the polarization by measuring the asymmetry for pp elastic scattering in Coulomb-nuclear-interference region, $1.5 \times 10^{-3} < t < 5.0 \times 10^{-2}$ (GeV/c)^2, where t representsthe four-momentum transfer squared. The asymmetry is theoretically calculated to be 4.6% at $t = 3.12 \times 10^{-3}$ (GeV/c)^2 [41]. The absolute polarization was determined comparing the measured asymmetry with the theoretical calculation [39].

The results were 40 $\pm$ 9 $\pm$ 15% (Primakoff polarimeter) and 45 $\pm$ 17% (CNI polarimeter) and were consistent with the results of the simulation of the polarized beam, 46%.

The momenta of the beam particles were determined from the angle deflected by the analyzing magnet (see Figure 7). The deflection angle was measured using MOM1, MOM2, and MOM3, which were segmented in the vertical direction. The tagged momentum spectrum is shown in Figure 10 (b). The tagged momentum was 198 $\pm$ 9 GeV/c, where 9 GeV/c is the root-mean-square.

Two threshold-type Cherenkov counters, 21.4-m long filled with helium gas at pressure of 0.3 atm, were used to separate protons from pions originating from K^0

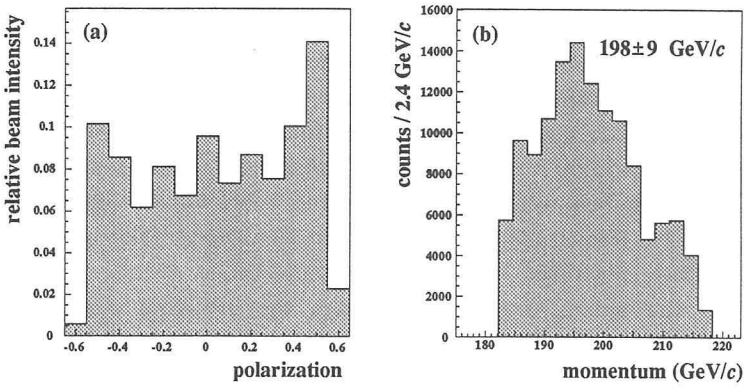

Fig. 10. (a) Ratio of the beam tagged in each polarization bin to the total beam.
(b) Momentum spectrum tagged by the momentum hodoscopes.

decays. The pressure of Cherenkov counters was set so as to reject pions with maximal efficiency. The contamination with pion in the beam was measured to be less than 0.1% using both of those counters.

2.1.3 Spin Rotation and Beam Definition

The spin-rotation magnets were located 300-m downstream of the production target (see Figure 11). The system comprised twelve dipole magnets. Each of them had a 10.2-cm gap, 22.9-cm aperture, and was 99.1-cm long. Applied magnetic field was 1.38 T. The pole faces of the magnets were tilted by $\pm$ 45° with respect to the vertical axis. Each magnet gave a spin rotation of 45° along the direction of the magnetic field.

Eight magnets out of twelve were used to rotate the proton-spin direction from the horizontal to the vertical direction which we needed in the measurement of the asymmetry A_N. The combination of magnet excitations was chosen so as to cancel both the bending angle and displacement of the trajectory of the beam particle when the beam passed through the spin-rotation magnets.

We installed two sets of hodoscopes, called "spin-rotator hodoscopes", upstream (SH1) and downstream (SH2) of spin-rotation magnets for tracking the beam as shown

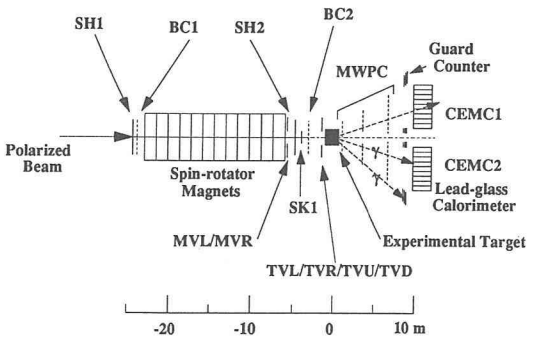

Fig. 11. Experimental apparatus downstream of the spin-rotation magnets.

in Figure 11. Each of them consisted of the x- and y-planes. The dimensions are listed in Table 3. These hodoscopes had an overlapping configuration similarly to the tagging hodoscopes shown in Figure 8. Beam chambers, BC1 and BC2, were also located 23-m and 2.2-m upstream of the experimental target, respectively, to detect the beam particle trajectory. Both of them comprised x- and y-planes. The wire-spacing of those chambers were 1 mm as shown in Table 4. Gas of 83% argon, 15% iso-butane, and 2% freon-13B1 which passed through the bubbler of cooled methylal were used for those chambers.

To reject the muons penetrating through the upstream materials, two veto scintillators, MVL and MVR, which had a hole of 7.8 cm in diameter around the beam axis were installed 4.65-m upstream of the experimental target. Using the four scintillators, TVL, TVR, TVU, and TVD, the beam particles which hit outside of the experimental target were rejected. Those scintillators had a hole of 2.57 cm in diameter and were located 1.81-m upstream of the experimental target. To provide a fast start signal for the time-of-flight (TOF) measurement, the scintillation counter, SK1, was installed 2.3-m upstream of the experimental target. The scintillator had a squared shape of 5 cm by 5 cm, and it was 3-mm thick. These scintillation counters were used for the beam definition as will be described later.

2.2 Detector System

In this subsection, we present the design and the performance of the detectors. The experimental apparatus downstream of the experimental target is shown in Figure 12. We used a liquid hydrogen target with a dimension of 5 cm in diameter and 100 cm in length. The density was stabilized within 0.2%. Main detectors of our experiment are central electro-magnetic calorimeters (CEMC) and photon detectors (guard counter) which surrounded the fiducial area of the calorimeters. A set of multi-wire proportional chambers (MWPC's) were installed for the detection of the charged particles as shown in Figure 12.

Table 3. Parameters of spin-rotator hodoscopes

Detector	Coordinate	Segment size (mm)	Sensitive area (mm^2)	Number of segments
SH1	x	2.00	55.0 × 55.0	27
	y	2.00	55.0 × 55.0	27
SE2	x	2.00	55.0 × 55.0	27
	y	2.00	55.0 × 55.0	27

Table 4. Parameters of beam chambers, BC1 and BC2.

MWPC	Coordinate	Wire spacing (mm)	Aperture (mm)	Number of wires
BC1	x	1.00	97.0	96
	y	1.00	97.0	96
BC2	x	1.00	97.0	96
	y	1.00	97.0	96

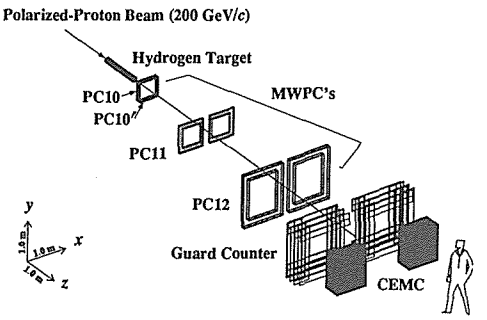

Fig. 12. Experimental apparatus downstream of the experimentaltarget.

2.2.1 *Central Electro-Magnetic Calorimeter (CEMC)*

We are interested in the high-p_T photon produced in the central region, $x_F \approx 0$, where x_F denotes the Feynman x-variable. We installed two sets of calorimeter whose front surfaces were located 10-m downstream of the experimental target on the left side (CEMC1) and the right side (CEMC2) of the beam axis, 1-m apart from the beam. The position corresponded to the polar angle of 90 degree in the center-of-mass system. The symmetric configuration was advantageous to cancel a possible asymmetry of the phase space of the beam at the target point. Each set comprised 504 lead-glass counters in an array of 21 by 24. The lead glass was referred to as TF1-000, which was fabricated at IHEP[3]. The radiation length was 2.50 cm. The characteristics of the lead glass are shown in Table 5 together with those of other lead glasses. It is shown that the optical properties of TF1-000 are similar to those of SF-5, but the content of PbO is different substantially. The Moliére radius[4] is around 3.3 cm. Each lead-glass block was wrapped with a sheet of alminized-mylar of 20-μm to increase the light-collection efficiency.

High capability to separate two showers close each other is indispensable for discriminating direct photons from high-p_T π^0's whose decay photons merge into one shower. The minimal distance, r, between two photons from the π^0 decay at the surface of the calorimeteris related to the p_T as shown in Equation (6). The minimal distances r are 9.9 cm and 6.2 cm at $p_T = 2.6$ GeV/c and 4.2 GeV/c, respectively. It

Table 5. Comparfson of parameters of lead glasses. The parameters, ρ , λ_{rad}, E_{crit}, and $R_{\text{Moliére}}$ denote the density, radiation length, critical energy, and Moliére radius, respectively.

type of lead-glass	ρ (g/cm^3)	λ_{rad} (cm)	index	PbO content (%)	E_{crit} (MeV)	$R_{\text{Moliére}}$ (cm)
TF1-000	3.86	2.50	1.67	65.4	15.8	3.32
SF-2	3.86	2.76	1.648	51	17.5	3.31
SF-5	4.08	2.54	1.673	55	15.8	3.38
SF-6	5.2	1.70	1.805	71	13.8	2.59

[3] Institute for High Energy Physics, Protvino, Russia

[4] The 99% of the energy is deposited within 3$\times$ $R_{\text{Moliére}}$, where $R_{\text{Moliére}} = (21\text{MeV})$. $\lambda_{\text{rad}}/E_{\text{crit}}$.

was desirable to use blocks of lead glass whose widths were smaller than r. The sizes of the calorimeter block were $3.81 \times 3.81 \times 45$ cm^3.

Photo-tubes

The Cherenkov photons generated in the lead glasses were detected with the photo-multiplier tube (PMT), PHEU-84-3, fabricated in Russia. Each PMT was optically connected to a block of lead glass using the silicon rubber as shown in Figure 13. The PMT had twelve-stage Venetian-blind type dinodes. The last four dinodes were fed by booster-power supplies to maintain the gain stability at high counting rate [42]. The photocathode was trialkaline of S-200 type (Sb-K-Na-Cs). It had the maximal sensitivity at 420 nm as shown in Figure 14. The wave-length distribution of the Cherenkov photons obeys the $(1/\lambda^2)$-law, where λ denotes the wave length. If this emission rate of photons was taken into account, the detection rate peaked at 385 nm. A programmable power supply, LeCroy HV 1440, was used as the high-voltage source for the PMT. The applied high-voltage was 1250 ± 50 V for the CEMC1 and 1240 ± 62 V for the CEMC2.

Assembling and Calibration

Each CEMC comprised 504 lead-glass counters in an array of 21 rows by 24 columns and two additional counters equipped with ^{241}Am-embedded NaI crystals for monitoring the system. These counters were mounted in a light-shielded box filled with nitrogen gas for cooling. The temperature was stabilized within $\pm$ 2°. Light from a light-emitting-diode (LED) was delivered to each lead-glass block via optical fibers to monitor the entire response of the lead-glass counter. This monitor system

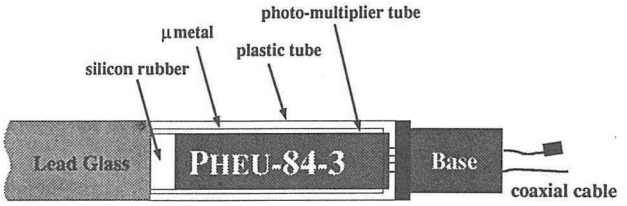

Fig. 13. Optical connection of a photo-tube (PHEU-84-3) and a block of the lead glass.

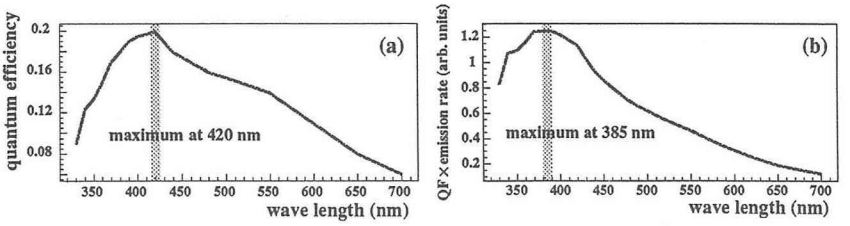

Fig. 14. (a) Quantum efficiency of the photo-tube PHEU-84-3 as a function of the wave length. (b) Quantum efficiency multiplied by the wave length distribution of Cherenkov photons.

ensured the gain stability within a few percent. The pulse height from each counter was digitized by LeCroy 2285A, whose full scale was 400 pC which corresponded to 12 bits. One ADC channel corresponded to about 25 MeV.

The whole system of each CEMC were put on the stage with the stepping-motor system, which controlled the position of the CEMC. All the counters were irradiated by the positron beams of 30 GeV/c in order to calibrate the energy. The incident position of the positron beam was measured using two beam chambers, BC1 and BC2, and additional chamber of the same type, BC3, which was located in front of the CEMC.

The energy resolution of 3.0% (r.m.s) and the spatial resolution of 1.5 mm (r.m.s) were obtained. Prior to this calibration, the entire calorimeter system was calibrated in IHEP at 10, 26.6, and 40 GeV. The linearity within 1% was obtained. As a result, we found the energy resolution as a function of energy to be

$$\frac{\sigma(E)}{E} = 1.0 + \frac{12.0}{\sqrt{E}}\,\%. \tag{9}$$

Here the E and $\sigma(E)$ represent the energy and energy resolution in GeV, respectively. During the calibration at IHEP, the response for hadrons was investigated using the pion beam of the same energies as the positrons. A rejection powerof 10^3 was obtained, hence the contamination by the hadrons in the shower detected in the CEMC was 0.1%.

The geometrical acceptances, η_{acc}, of each CEMC for π^0 detection and for γ detection are shown in Figure 15. Here η_{acc} is calculated by Monte Carlo simulations. In the case of π^0 both decay photons are required to be accepted. The η_{acc} is 10.5% for the π^0 produced in $\mid x_F \mid < 0.1$ and at $p_T = 2.5$ GeV/c, whereas it is 13.1% at 4.1 GeV/c in the same x_F region.

2.2.2. *Guard Counter*

The detection of the direct photon suffers from huge backgrounds from neutral meson decays such as $\pi^0 \rightarrow \gamma\gamma$ and $\eta \rightarrow \gamma\gamma$. If one of the decay photons has a high-p_T and the other misses the CEMC, the high-p_T photon will fake a direct photon. To reject such events, we extended the fiducial area of photon detection by installation of additional photon detectors called "guard counter".

The guard counter consisted of three layers of plastic scintillator and two layers of

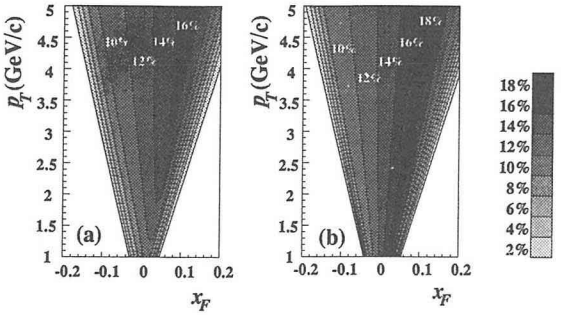

Fig. 15. Geometrical acceptance for (a) π^0 detection and for (b) γ detection as a function of x_F and p_T presented as contour plots.

lead inserted between the scintillators. The plastic scintillators were 5-mm thick and the lead plates were 12.5-mm thick. The guard counter surrounded the fiducial area of each CEMC like a picture frame. Each side was divided into two pieces lengthwise as shown in Figure 16. The dimensions of the scintillators are summarized in Table 6. The width of the scintillator was chosen to reduce the ratio of the number of fake photons mentioned above to the number of π^0's to a few percent according to the Monte Carlo simulation. Figure 17 shows the ratio as a function of width of the scintillator. As a result, the fiducial area for the photon detection was four times as large as that of the CEMC. Figure 18 shows the fiducial area of the CEMC and the guard counter both in the laboratory system and in the center-of-mass system (c.m.s.). The transformation to the c.m.s. was done for a photon. In the figure, p_x and p_y denote the momenta of photon in x- and y-directions. The x_F denotes the Feynman x-variable and x_T is defined as,

$$x_T = \frac{2p_T}{\sqrt{s}}. \tag{10}$$

The fiducial area is significantly extended by installation of the guard counter. The efficiency of photon detection was measured at INS[5] using tagged photons at several energy points from 150 MeV to 890 MeV and found to be greater than 98%.

Each scintillation counter was viewed by the PMT's, HAMAMATSU H-1161 from

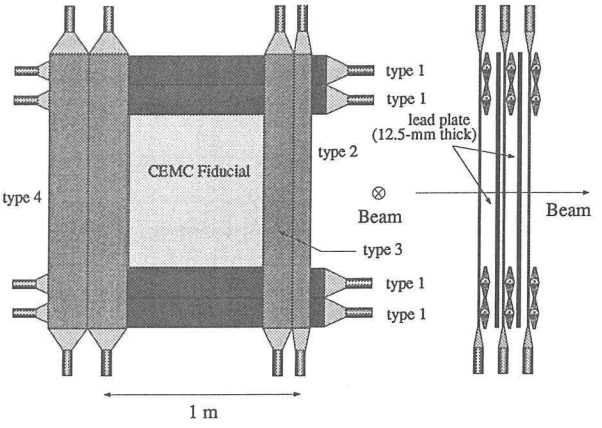

Fig. 16. Front view and side view of the guard counter.

Table 6. Sizes of plastic scintillators of the guard counter.

	x(cm)	y(cm)	z(cm)
type 1	135.4	15.0	0.5
type 2	9.0	140.0	0.5
type 3	15.0	140.0	0.5
type 4	20.0	140.0	0.5

[5] Institute for Nuclear Study, University of Tokyo.

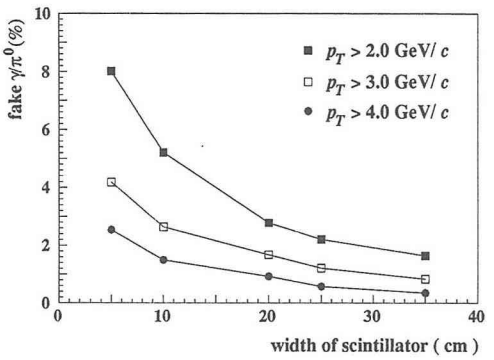

Fig. 17. Ratio of the number of the fake direct photons to the number of π^0's as a function of the width of the scintillatorobtained by the Monte Carlo simulation.

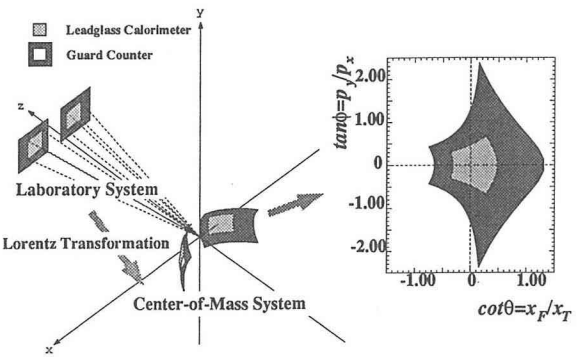

Fig. 18. Fiducial area of the CEMC and the guard counterin the laboratory system and in the center-of-mass system. The transformation has been done for a photon.

both ends. The PMT has twelve stages of dinode of linear-focus type. The most downstream layer provided timing information as well as pulse-heights, while the other layers provided only pulse-heights. The time-to-digital-converter (TDC) module used for the counter was REPIC RPC-060, whose full range was 100 nsec which corresponded to 12 bits. The analog-to-digital converter (ADC) module used was LeCroy 2285A, whose full scale was 400 pC which corresponded to 12 bits.

2.2.3 Detection of Tracks of Charged Particles

The tracks of outgoing charged particles were detected using the four sets of MWPC's, PC10, PC10′, PC11, and PC12. The PC11 and PC12 comprised two identical sets on the left and right sides of the beam axis as shown in Figure 12. The azimuthal angles of wire directions were 0.0°, 90.0°, 28.1°, and −28.1° for x, y, u, and v planes, respectively. The gas used for PC11 was the mixture of 99.7% argon and 0.3% freon which passed through the bubbler of cooled methylal. The gas of argon-CO_2 mixture with freon-13B1 was used for PC10, PC10′, and PC12. A typical detection efficiency of each plane of MWPC's was about 85%.

2.3 *Trigger and Data Acquisition*

The experiment focused on the spin effects in the high-p_T phenomena of which the cross section is significantly small. To select the high-p_T events, we used a special trigger scheme "High-p_T trigger". The event-trigger logic is described first and the description of the data acquisition system follows.

2.3.1 *Triggering System for High-p_T Events*

The triggers consisted of two parts, "Good Beam" signal for beam definition and "High-p_T" signal for physical requirements as summarized in Figure 19.

Beam Definition–"Good Beam" Signal

The "Good Beam" signal was a combined logic as follows;

$$\text{Good Beam} = \text{TB}\bar{\text{E}}\,\bar{\text{S}} \otimes \text{Good Mom} \otimes \text{USB} \otimes \text{SK 1} \otimes \overline{\text{Veto}}. \qquad (11)$$

Here the " $\text{TB}\bar{\text{E}}\,\bar{\text{S}}$ " signal indicates that the current beam particle was separated from the preceding particles at least by 60 nsec which ensured the tagging logic was ready to allow the tagging of the current beam particle. The "Good Hit" signal indicates that the event caused a single hit in each of the five hodoscopes used for tagging the beam particles (see Section 2.1.2). The "Good Mom" signal indicates that the momentum of the current particle was within the programmed momentum bite, $\pm$ 9%. The "USB" (Usable Spin-rotated Beam) signal was generated when the the current particle

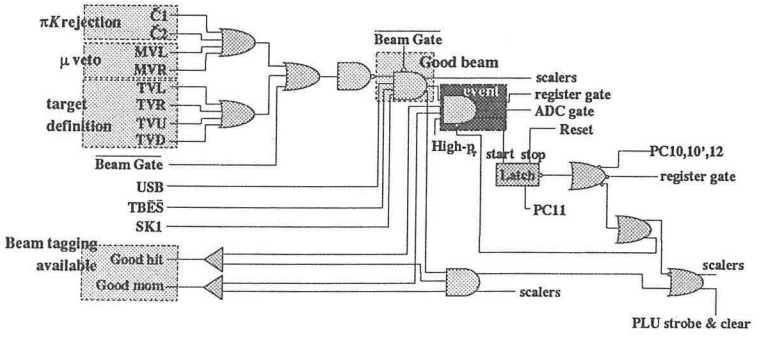

Fig. 19. Diagram for the event trigger logic. The event trigger consisted of "Good Beam" signal and "High-p_T" signal.

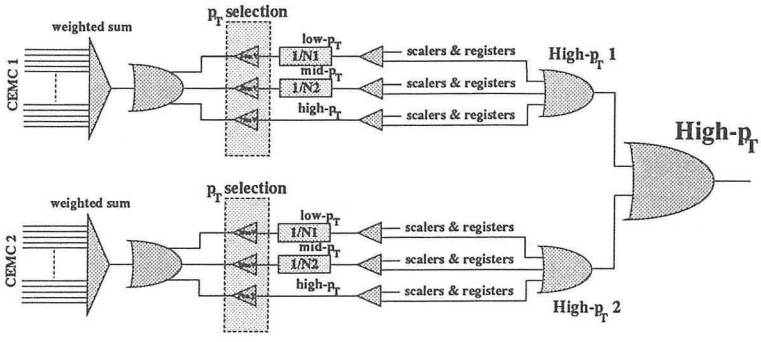

Fig. 20. Diagram for "High-p_T" signal.

caused one or two hits in each of the four spin-rotator hodoscopes. The "SK1" signal indicates that the beam particle hit the scintillation counter, SK1. This signal had the narrowest width among the signals for event definition, and was used in order to determine the timing of the event gate. The "Veto" signal was generated as

$$\text{Veto} = \check{C}_1 \oplus \check{C}_2 \oplus \text{MVL} \oplus \text{MVR} \oplus \text{TVL} \oplus \text{TVR} \oplus \text{TVU} \oplus \text{TVD}. \quad (12)$$

The "$\check{C}_1$" and "$\check{C}_2$" signals indicate that the current particle generates more Cherenkov photons in two Cherenkov counters than the applied threshold. The "MVL" and "MVR" signals indicate that the current beam particle hit the scintillation counters, MVL and/or MVR which were installed for μ rejection as shown in Figure 11. The "TVL/TVR/TVU/TVD" signal occurred when the beam hit the target defining counter. Any of these signals vetoed the beam definition signal.

"High-p_T" Signal

Electronic signals whose pulse heights were approximately proportional to the transverse momenta of electromagnetic showers in each CEMC were utilized to trigger the events with high-p_T. The signals were given as weighted sums of the pulse heights of signals from the lead-glass counters. Different weights were given for every column of the calorimeter array. The relative weights are shown in Figure 21(a). The weight was determined so that those are proportional to $\sin\theta$ at $Iy = 0$, where θ is the polar angle and Iy is the raw number in y-direction defined in Figure 21 (c). Consequently, the deviation from the real p_T increases up to 30% at the innermost counters as shown in Figure 21 (b).

The threshold voltage applied to the "High-p_T" signal was 70 mV for both CEMC's which corresponded to about 2.1 GeV/c. The efficiency of this trigger is shown as a function of p_T in Figure 22. As is seen in the figure, the trigger efficiency is higher than 98% in the p_T region above 2.5 GeV/c.

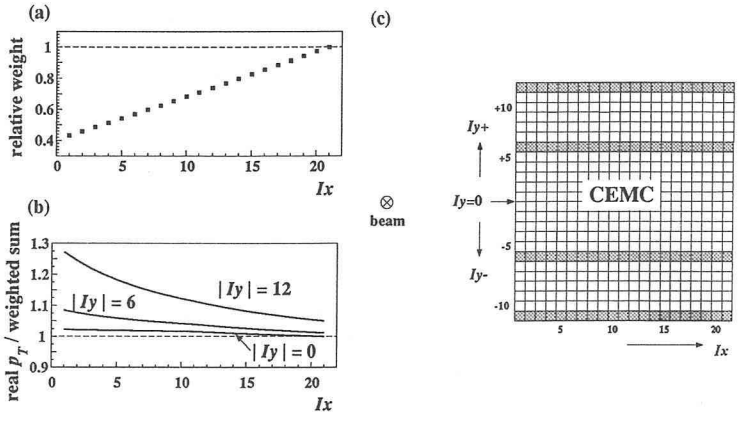

Fig. 21. (a)Relative weight for the generation of "High-p_T signal. The coordinate system is defined as shown in (c), where Ix and Iy indicate the counter numbers in x-and y-directions, respectively. (b)Ratios of the real p_T to the weighted sums are plotted for the shaded raws in (c).

2.3.2 *Data Acquisition and On-line Monitoring*

The data acquisition (DAQ) system, the monitoring system, and the diagram of the data flow are schematically shown in Figure 23. The DAQ system was constructed on the basis of the PDP-11. According to the types of trigger, the data were collected from the CAMAC modules. The data were sent to the magnetic-tape recorder (6250 bpi) from PDP-11. The quality of the data was monitored using the on-line analysis software built on the VAX station 3200. The samples of the data were sent to the VAX through the DR11-link from the PDP-11.

A typical polarized-beam intensity was 2×10^7 per spill. The computer live efficiency was 80% at the event rate of 15 events/sec correspondingly.

Integrated Luminosities

The integrated luminosities for the direct-photon production and for the π^0 production are calculated as

$$\int \mathcal{L} dt = N_B \frac{N_{Av} p}{A} \int_0^{\Delta z} e^{-\frac{z}{\lambda}} dz. \tag{13}$$

Here $\int \mathcal{L} dt$ denotes the integrated luminosity. The N_B represents the number of

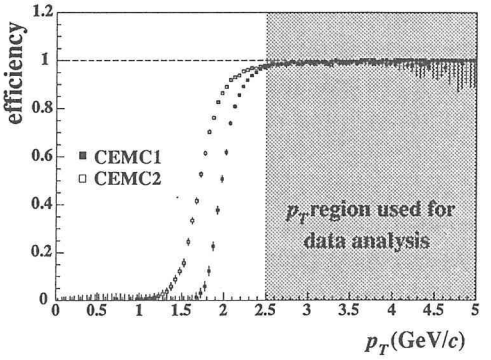

Fig. 22. Efficiency of the "High-p_T trigger" as a function of p_T for each CEMC.

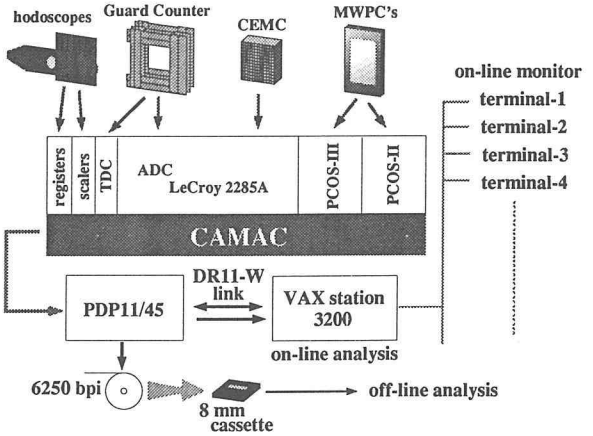

Fig. 23. Diagram of the data flow in the data acquisition and monitoring system.

beam particles, N_{Av} is Avogadro's number, ρ is the density of the liquid-hydrogen target, and A represents the atomic number of hydrogen. The effective number of the beam particles is N_B multiplied by $\int_0^{\Delta z} e^{-\frac{z}{\lambda}} dz$, where z represents the position in the beam direction, Δz is the length of the target, and λ is the nuclear interaction length. The number of the beam particles for each status of the spin-rotation magnets and for each polarization bin are summarized in Table 8. In the status I, the spin of the positively-polarized proton was rotated to "up" and the negatively-polarized proton was rotated to "down". The status II provided the opposite spin direction. During the status III, the current setting of the spin-rotation magnets was being changed, and the polarization of the beam particles was undefined. The beam during status III, however, has been used for the analysis of the cross sections, because the average polarization was zero. We have used the data after the installation of the MWPC's for the analysis of the direct-photon production. The evaluation of the background contribution from neutral mesons has been done using the same data set. We have extended the data set to determine the cross section for π^0 production in better precision including the data in which the MWPC's have not been available.

The integrated luminosities are 141 nb^{-1} for direct-photon runs and 257 nb^{-1} for π^0 runs, respectively.

Table 7. parameters of MWPC's downstream of the target. The PC11 and PC12 consisted of two identical sets on the left and right sides of the beam axis.

MWPC	Coordinate	Wire Spacing (mm)	Aperture (mm)	Number of Wires	Distance from the Target(m)
PC10	x	2.00	514.0	257	1.0
	y	2.00	514.0	257	
PC10′	x	2.00	514.0	257	1.1
	y	2.00	514.0	257	
PC11	x	1.95	500.0	256	3.4
	y	1.95	500.0	256	
	v	1.95	627.0	320	
PC12	y	2.00	1026.0	512	6.6
	u	2.00	1026.0	512	
	v	2.00	1026.0	512	
	x	2.00	770.0	384	

Table 8. Number of polarized-beam particles during direct-photon runs and π^0 runs. The sign " + (−)" represents the number of positively (negatively) polarized particles in the beam, while "0" indicates unpolarized particles in the beam. The spin-rotator status I and II represent the current settings with opposite polarities each other. The polarity is being changed during stagus III.

spin-rotator	direct-photon run ($\times 10^9$)				π^0 run($\times 10^9$)			
status	+	−	0	subtotal	+	−	0	subtotal
I	3.60	3.22	8.08	14.91	6.51	5.55	14.36	26.42
II	3.64	3.17	8.10	14.92	6.64	5.54	14.53	26.70
III	1.40	1.20	3.08	5.67	2.82	2.34	6.17	11.33
total	8.64	7.59	19.27	35.49	15.96	13.43	35.06	64.46

3 Data Analysis

The data on the events obtained in this experiment include the following information:

- energies and positions of the showers detected in the CEMC,
- charged tracks and the event vertex obtained from the MWPC data,
- positions of hits in the guard counter in proper timing with the flag of charged or neutral particles.

This section describes the procedure to derive those event information.

3.1 CEMC Data

In this subsection, the reconstruction of the 4-momenta of photons from the energy deposits observed in the calorimeters is described. This reconstruction procedure has been made on a basis of the function minimization. The function to be minimized is the parameter representing the deviation of observed energy depositsfrom "*shower reference table*", which contains average energy deposits in each lead-glass block.

3.1.1 "Shower Reference Table"

The "*shower reference table*" has been made using the data obtained with 30-GeV positron beams. We have measured the incident positions of the positrons on the front surface of the CEMC with MWPC's and the energy deposits in each lead-glass block of the CEMC. We have learned from the data that most of the energy has been deposited in 3×3 blocks. The "*table*" gives the relation between the incident position and the energy deposits in the 3×3 blocks.

The front surface of the lead-glass block has been divided into 25×25 small domains called "*sub-cell*" whose sizes are 0.152×0.152 cm^2. The "*table*" was obtained for incident positrons on each "*sub-cell*", where the numerical values in the "*table*" show the fractions of the energy deposits in each of the 3×3 blocks of interest. Energy leakage of the shower from the 3×3 blocks was ignored in obtaining the "*table*", because the energy deposit outside the 3×3 blocks was smaller than a few percents of total energy of the shower.

When a positron is incident on the center of a lead-glass block, 81% of the energy is deposited in the block.

3.1.2 Shower Reconstruction

Figure 24 shows the flow chart of the algorithm for shower reconstruction. Before the shower reconstruction has been carried out, the energy deposits less than 75 MeV have been eliminated and isolated energy deposits without any energy deposit in a contiguous block have been deleted.

The shower reconstruction has been started from the lead-glass block with the maximum energy deposit. Clustering procedure is applied for the blocks around it to form a group of energy deposits which are contiguous each other. If the energy sum for the cluster is below 0.5 GeV, the procedure terminates. Otherwise, the center of gravity $(\bar{x}, \bar{y})$ and the variances (σ_x^2, σ_y^2) are calculated in each of x and y direction. If

the cluster size is equal or less than 3×3 blocks, the cluster is considered as one shower. Actually the center of gravity does not directly give the incident position of the shower. The position correction function, which relates the center of gravity and the incident position has been made prior to the shower reconstruction as shown in Figure 25. Accordingly the x and y coordinates are corrected and the residual ρ is calculated, where the ρ is defined as

$$\rho = \frac{\sum_i (E_i^{data} - E_i^{table})^2}{\sum_i E_i^{data}} \quad \text{(GeV)}. \tag{14}$$

Here E_i^{data} represents the energy detected in the i-th counter and E_i^{table} stands for the energy calculated for the i-th counter using the "*shower reference table*" and the total energy deposit, $\sum_i E_i^{data}$.

The total energy deposit, E, is related to the number of detected photo-electrons, N_{pe}, as $E = C \cdot N_{pe}$, where the fluctuation dE is approximated to be $C \cdot \sqrt{N_{pe}}$. The constant C is about 0.001 GeV per photo-electron. The N_{pe} in i-th counter, N_{pe}^i ($\sum_i N_{pe}^i = N_{pe}$), is also fluctuated by $\sqrt{N_{pe}^i}$, and the ρ is approximated as

$$\rho = \sum_i (dE)^2 / \sum_i E \tag{15}$$

$$= \sum_i (C \cdot \sqrt{N_{pe}^i})^2 / \sum_i C \cdot N_{pe}^i \tag{16}$$

$$= C. \tag{17}$$

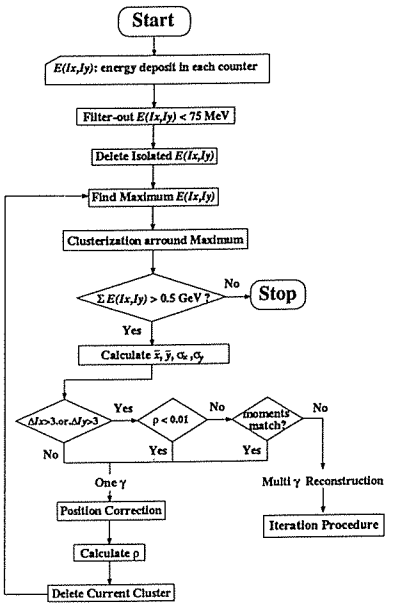

Fig. 24. Flow chart of the algorithm for the shower reconstruction. Here $E(Ix, Iy)$ denotes the energy deposit in the counter labeled by Ix ($1 \leq Ix \leq 21$) and Iy ($1 \leq Iy \leq 24$). ΔIx and ΔIy represent the cluster sizes in x-and y-directions.

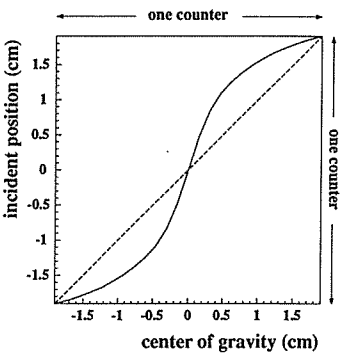

Fig. 25. Position-correction function which relates the center of gravity and the incident position. The origin corresponds to the center of the lead-glass block. The dashed line corresponds to the case without any correction.

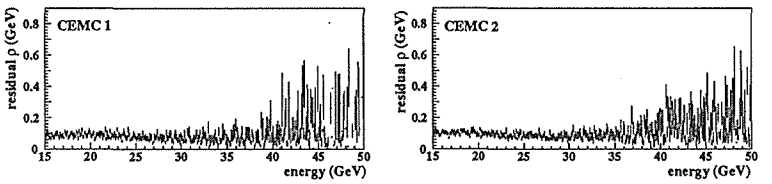

Fig. 26. Mean value of residual ρ is plotted as a function of the shower energy for CEMC1 and CEMC2. The error bars indicate the root-mean-square of ρ in each energy bin.

Hence, ρ is independent of energy at the first approximation, though it has the dimension of energy. In Figure 26, the averaged ρ for real datais plotted as a function of energy. The error bars indicate the root-mean-square of ρ in each energy bin. The plot shows that ρ is approximately independent of energy.

Even for the cluster larger than 3×3 blocks, the cluster is treated as one shower, if the cluster has ρ less than 0.01 GeV, as described above. Otherwise the cluster is treated as two or more showers.

An iteration procedure to minimize ρ is applied for overlapped two showers. Here the parameters to be determined are six variables, E_i, x_i, and y_i $(i = 1, 2)$. First the iteration is carried out for the spatial coordinates with the fixed energies, that is $E_1 = E_2 = 0.5 \times \sum_i E_{data}$. The initial positions are taken as

$$x_1 = \overline{x} + \sqrt{\sigma_x^2}, \tag{18}$$

$$x_2 = \overline{x} - \sqrt{\sigma_x^2}, \tag{19}$$

for x-positions and y-positions are determined in a similar manner. These initial positions are determined assuming that the parameters, $\overline{x}$, $\overline{y}$, σ_x^2, and σ_y^2, calculated from the energy deposits in the cluster are equal to the ones calculated from the six parameters, e.g.,

$$\overline{x} \equiv \frac{\sum E_i^{data} x_i^c}{\sum E_i^{data}} = \frac{E_1 x_1 + E_2 x_2}{E_1 + E_2}. \tag{20}$$

Here x_i^c denotes the position of the lead-glass block in x-direction. This assumption works well because the width of the shower is sufficiently narrow. The values of the parameters with which ρ is minimized are determined with this assumption.

After the iterations on spatial coordinates have been done, the energies are released from the initial values, and the iterations on all the six parameters are made. The procedure terminates under the following conditions;

- the minimal ρ has been found,
- the difference between the current values and the previous values of the parameter is less than 1% of the counter size for spatial coordinates and also of the total energy for the energy parameters,
- the number of iterations becomes ten.

3.2 Reconstruction of Charge Tracks

The track-reconstruction procedure to obtain the tracks of charged particles from

the hits in MWPC's is based on the least-χ^2 method. Since we had no magnetic field between the target and the detectors, charged particles made straight tracks. A straight track is expressed as the relation between the z-coordinate and one of the x, y, u, and v coordinates as

$$\xi = (Az + B)\cos\phi_\xi + (Cz + D)\sin\phi_\xi, \quad (\xi = x, y, u, \text{and } v) \tag{21}$$

where ϕ_ξ denotes the rotation angle of the ξ-plane. Here A, B, C, and D are fitting parameters. The χ^2 is defined as

$$\chi^2 = \sum_i \sum_{\xi i} \left[\frac{\xi_i^{data} - \{(Az + B)\cos\phi_{\xi i} + (Cz + D)\sin\phi_{\xi i}\}}{\Delta\xi_i}\right]^2$$

Here the sum is taken over i, which stands for each MWPC, and ξ_i, which represents the x, y, u, and v coordinates. The $\Delta\xi_i$ denotes wire spacing in the ξ_i-plane. The fit parameters A, B, C, and D have been determined by minimizing χ^2. In this procedure, we have required that at least one plane of PC10, one plane of PC10′, two planes of PC11, and three planes of PC12 should have hits. In order to improve the tracking efficiency, we have applied another procedure additionally, which is actually not based on the least-χ^2 method. If the two planes in both of the most downstream two chambers, PC11 and PC12, have a hit, the parameter A, B, C, and D are determined. Then we have required at least one hit in PC10 which has matched the hit position predicted by the determined parameters.

The track-finding efficiency has been obtained as follows. As mentioned in the previous section, the guard counter provides timing information and pulse-height information. From the pulse heights in the most upstream layer, we can tell whether the particle traversing the guard counter is charged one or not. Timing information is used to ensure that the particle hits the guard counter in proper time. We have defined N_{charge}^{GC} as the number of charged particles detected in the guard counter in proper time. Then we have tried to find the tracks of the charged particles which have passed through the guard counter using the MWPC's. Actually the guard counter was not fully covered by the sensitive area of the MWPC's. The coverage, η_{cover}, ranged from 5.4% to 93.5% depending on the scintillation counter of the guard counter. The number of the charged tracks on the guard counter, N_{track}^{GC}, has been divided by N_{charge}^{GC} and η_{cover} to obtain the track finding efficiency. The tracking efficiencies are $(32\pm3)\%$ on the left side and $(31\pm3)\%$ on the right side.

The event vertex has been reconstructed using the outgoing charged tracks and the beam track obtained by BC1 and BC2. If the beam tracking has been unavailable due to the inefficiency of the beam chambers, the beam track has been determined using the hit on the "spin-rotator hodoscopes", SH1 and SH2. The efficiency of the track determination with those hodoscopes is almost 100%, because the hit on these hodoscopes are required in the event trigger. Consequently, the vertex finding efficiency has been determined mostly by the track finding efficiency for the charged tracks downstream of the experimental target.

In the evaluation of the vertex finding efficiency, we have selected the events with at least one combination of two showers whose invariant mass has been consistent with that of π^0. The number of such events is denoted by N^{π^0}. In most of such events,

we have expected at least one charged particle emitted from the target according to the PYTHIA simulation. Among the events selected as above, the number of the events with vertex has been defined as $N^{\pi 0}_{vertex}$. The vertex finding efficiency, ϵ_{vertex}, has been evaluated as

$$\varepsilon_{vertex} = \frac{N^{\pi 0}_{vertex}}{N^{\pi 0}} \tag{22}$$

The vertex finding efficiency has been found to be $33 \pm 3\%$.

Figure 27 shows the invariant mass spectrum of charged particle pairs which matches with the showers detected in the CEMC within 2.0-cm apart each other. The peak at 3130.4 ± 26.8 MeV/c^2 has been identified as the $e^+ e^-$ pairs from the J/ψ decay. It demonstrates that the reconstructions of the charged tracks in MWPC's and the showers in the CEMC have been performed sufficiently well.

3.3. Particle Hit on Guard Counter

The most downstream layers of the guard counters provide timing information as well as pulse height information. Timing information has been used for rejecting possible back-splash from the CEMC located 1-m behind the guard counters, and for obtaining hit positions of particles on the guard counters.

The scintillation light was detected with the PMT's at the both ends of the scintillator. Those two pulse heights, $\mathcal{A}_1$ and $\mathcal{A}_2$, are given as a function of d_1 and d_2, the distances from the hit positions to the surfaces of the PMT's as:

$$\mathcal{A}_i(d_i) = \mathcal{A} \cdot \exp(-d_i/\lambda_{att}) \quad (i = 1,2), \tag{23}$$

where $d_1 + d_2 = L$ is the distance between the two PMT's. The parameter λ_{att} represents the effective attenuation length. Figure 28 shows the scatter-plots of the pulse heights versus hit positions in x-direction obtained with MWPC's. We have fit the pulse height to Equation (23) to obtain the attenuation length. The averaged attenuation lengths are listed in Table 9 for each type of scintillation counter except

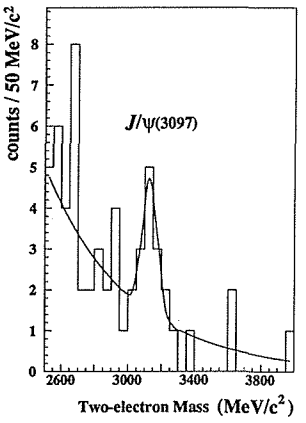

Fig. 27. Invariant mass spectrum of charged particle pairs, which match with the showers detected with the CEMC's in positions. The mass has been calculated on the assumption that the showers have originated from electrons.

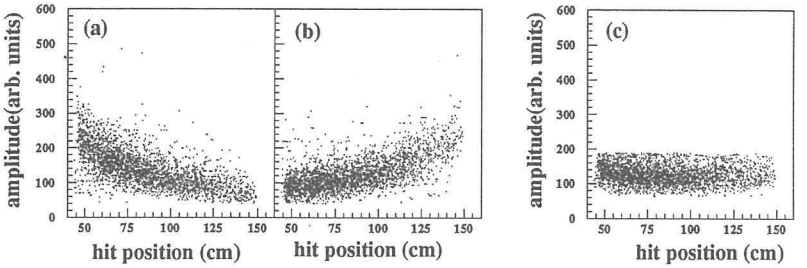

Fig. 28. Position dependence of ADC counts (a) from PMT at the left end and (b) at the right end. The geometrical mean of those pulse heights is almost independent of the hit position as shown in (c).

Table 9. Performance of the guard counters.

	attenuation length(cm)		time resolution(nsec)		position resolution(cm)	
	mean	r.m.s.	mean	r.m.s.	mean	r.m.s.
type 1	87.5	7.6	0.69	0.08	7.20	1.77
type 3	82.9	6.0	0.71	0.00	10.40	0.65
type 4	93.0	6.6	0.74	0.03	10.26	2.04

type 2 which was not covered by the set of MWPC's (see Table 6).

As easily expected from Equation (23), the geometrical mean of both pulse heights is expected to be independent of the hit position. Figure 28 (c) demonstrates the validity of the simple expectation. And we have used geometrical mean as a position-independent pulse height. Figure 29 shows a typical pulse height spectrum.

Timing information depends on the hit position of the particle as well as the amplitude due to the "*slewing effect*". The correction on timing, Δt_i, follows approximately the formula:

$$\Delta t_i = \frac{d_i}{v_{eff}} + \frac{\alpha}{\mathcal{A}_i}. \tag{24}$$

Here d_i is the length between the hit position and the PMT surface, v_{eff} is the effective speed of light traversing the plastic scintillator,and $\mathcal{A}_i$ represents the amplitude detected with the PMT. The fit parameters are v_{eff} and α. For determination of those parameters, events with a reconstructed track of charged particleon the guard counters have been selected, because in such events the hit position, x, has been known. The timing data have been fit to Equation (24) for correctionas shown in

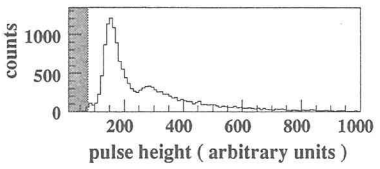

Fig. 29. Typical pulse height spectrum for a segment of the guard counter.Here the geometrical mean of the pulse heights from both ends of the segment is taken to eliminate the position dependence. The gray region on the left indicates the pedestal region which is treated as "no hit" in the segment.

Figure 31 (b). The effective speed of light v_{eff} has been obtained as 13.16 ± 1.27 cm/nsec, which has been almost consistent with our expectation.

A typical timing resolution has been found to be 0.7 nsec (r.m.s.), which is sufficient for rejection of possible back-splash from the CEMC located 1-m behind the guard counter. The spatial resolution has been about 9 cm (r.m.s.). Those resolutions have been obtained for charged particles. We have assumed the same resolution for photons in the analysis.

Using timing and pulse height information, we have defined the photon-like hit as the hit in proper timing without any pulse in the first layer. If there has been a pulse in the first layer, the hit has been considered as a charged particle. This criterion has been used in obtaining the tracking efficiency as mentioned in the previous section.

4 π^0 Production

We describe the procedure to extract the number of π^0 mesonsfrom the data and the efficiency of our method in this section.

4.1 Extraction of π^0 Mesons

Figure 32 shows the invariant mass spectra for any combination of two showers with the residual $\rho < 0.3$ GeV and $\mathcal{A}_E < 0.8$. Here $\mathcal{A}_E$ represents the energy

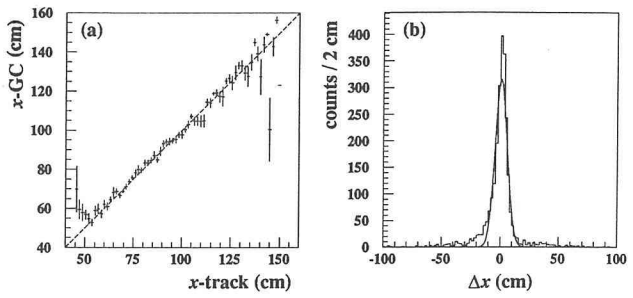

Fig. 30. (a) The x-position determined using MWPC's (x-track) versus the x-position determined from the time measurement onthe third layer of the guard counter (x-GC). (b) Difference of two x-positions. A spatial resolution of 5.15 cm has been obtained for the segment.

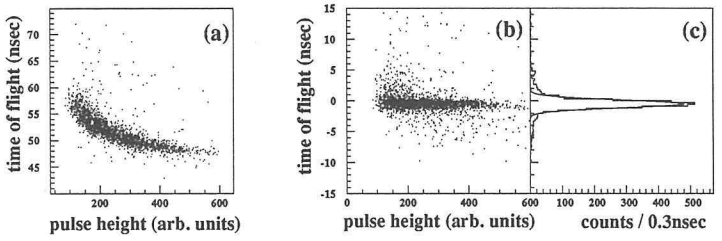

Fig. 31. Scatter plot of (a) uncorrected time-of-flight (TOF) versus pulse height and (b) corrected TOF versus pulse height and (c) the projection for TOF spectrum.

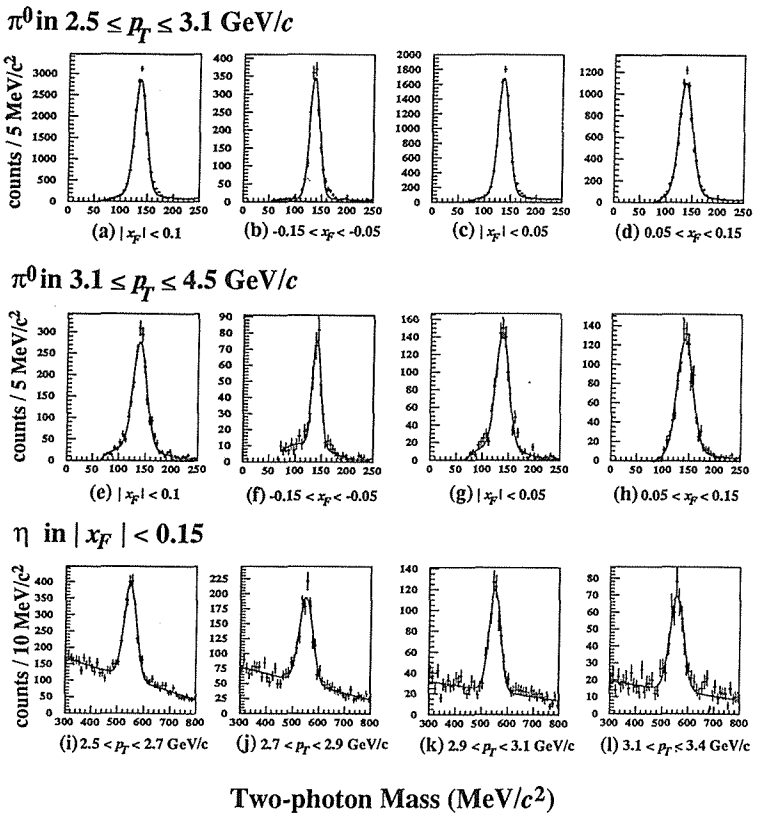

Fig. 32. Two-photon mass spectra at $2.5 \le p_T \le 3.1$ GeV/c((a)-(d)) and $3.1 \le p_T \le 4.5$ GeV/c ((e)-(h)) for π^0-mass region and those for η-mass region in selected p_T bins ((i)-(l)).

asymmetry of two showers, $|E_1 - E_2| / (E_1 + E_2)$ [6]. The cut on $\mathcal{A}_E$ reduces the combinatorial backgrounds. The mass spectra for $2.5 \le p_T \le 3.1$ GeV/c with different x_F bins are shown in Figure 32 (a)-(d) and these for $3.1 \le p_T \le 4.5$ GeV/c in Figure 32(e)-(h). The spectra for the η-mass region at $|x_F| < 0.15$ with selected p_T bins are shown in Figure 32(i)-(l). The number of π^0 mesons has been obtained by fitting the data to an empirical form, Gaussian distribution for the signal plus the third polynomial distributionfor the combinatorial background. The same procedure has been applied to obtain the number of η mesons.

4.2 Reconstruction Efficiencies

The efficiency of π^0 reconstruction is determined bya Monte Carlo simulation using the simulation packages of PYTHIA 5.4 [43] and GEANT 3.15 [44]. A subroutine to generate Cherenkov photons in the CEMC has been included in the GEANT. The number of Cherenkov photons has been calculated from the velocity of the charged particle generated by GEANT and the attenuation of photons in the lead glass. The

[6] $\mathcal{A}_E = \beta|\cos\theta|$, where θ is the decay angle in the π^0 rest frame and β is the velocity of the π^0 in the laboratory frame; since the π^0 has spin 0, the decay distribution should be flat in $\cos\theta$.

attenuation length λ_{att} has been chosen to reproduce the calibration data with respect to the energy resolution, the "*shower reference table*", and the ρ distribution[7]. Finally we have chosen $\lambda_{att} = 38$ cm correspondingly to the wave length at the maximal detection, that is 385 nm (see Section 2. 2. 1). Actually we have developed another subroutine which has included the wave length distribution of the Cherenkov photon, the quantum efficiency of the PMT, and the measured dependence of attenuation length on the wave length. In this simulation, total reflection is required for all the generated photons. The simulation has given similar results as the one with simpler simulation described above, while it has invested extensive CPU time. Therefore, we have employed the former simulation. The resulting "*shower reference table*" is compared to the one from the real data in Figure 33. The simulation has reproduced the "*shower reference table*" well, though the decrease of the value with the increase of c_x has been a little more rapid than in the real data. Here c_x is the label for the "*sub-cell*" in x-direction, which is defined in Section 3. The origin of the label is taken at the center of the lead-glass block. The rapid decrease is caused by a slightly narrower shower width in the case of the simulated data.

In Figure 34, the mass spectra for two photons and the ρ distribution for the calibration data are compared to the data simulated using GEANT. It should be noted that the cut with $\rho < 0.3$ GeV results in the efficiency of 95% in both of the calibration data and the simulated data.

The generated events with PYTHIA 5.4 have been sent to GEANT to produce simulated showers in the CEMC. The number of photons have been digitized for each counter as in the case of the real data. The generated data have been processed

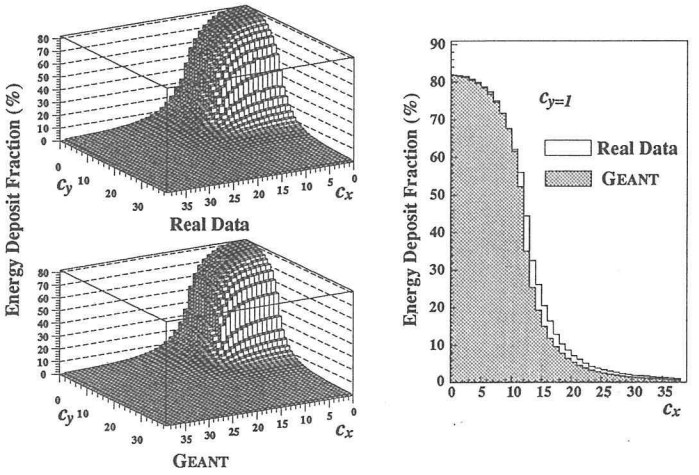

Fig. 33. Comparison of real data and GEANT simulation in "*shower reference table*". Here c_x and c_y are the labelsfor the "*sub-cell*" defined in Chapter 3. The origin is taken at the center of the lead-glass block. The plots show a quarter of the "*table*". Histograms show the comparison in the slice at c_y=1.

[7] The "*shower reference table*" is sensitive to the shower shape. The ρ distribution reflects the fiuctuation of the shower.

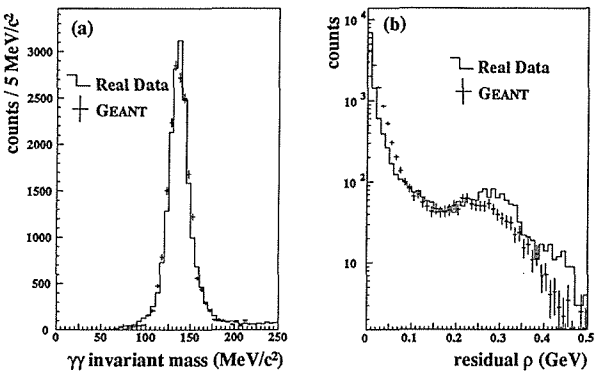

Fig. 34. Comparison of real data and GEANT simulation in (a) two-photon mass spectra and (b) residual ρ distribution.

through the completely same algorithm as the one for the real data. The number of the identified π^0 has been divided by the number of the generated π^0 accepted in the fiducial area in order to obtain the reconstruction efficiency.

The obtained efficiencies are shown in Figure 35(a). The error bars indicate the statistical errors of the simulated data. The dashed line shows the maximum efficiency where the inefficiency is due to the energy asymmetry cut, $\mathcal{A}_E < 0.8$. The cut, $\rho < 0.3$ GeV, for both showers contributes to the efficiency by 0.95×0.95. Besides, the shower positions in the x-direction reconstructed by the algorithm is shifted to outside by about 0.5 counter (1.9 cm) due to the incident angle which is different from normal at the position of the surface of the CEMC. This leads to additional loss of the efficiency of 5%. The decrease of the efficiency at higher p_T is due to the decrease of the separation efficiency at short distance. The separation efficiency is plotted as a function of the distance of the two showers in Figure 35(b).

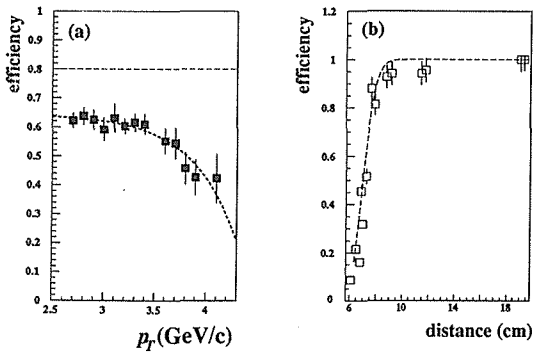

Fig. 35. (a)Reconstruction efficiency as a function of p_T. (b)Separation efficiency for two showers as a function of the distance of two showers induced by two photons of 10 GeV.

Geometrical Acceptance

Figure 36 shows the geometrical acceptanceof the CEMC, η_{acc}, for the π^0 detection as a function of p_T in $|x_F|<0.1$ and $|x_F|<0.15$. Here we have employed two types of x_F distributions, a flat x_F distribution and the distribution determined experimentally in Reference [45] as

$$E\frac{d^3\sigma}{dp^3}=A\cdot\frac{(1-x_D)^F}{(p_T^2+m^2)^N}. \tag{25}$$

Here x_D is defined as,

$$x_D=\sqrt{(2p_T/\sqrt{s})^2+(x_F-x_0)^2}. \tag{26}$$

The fitting parameters are $A=(0.122\pm0.015)\times10^{-25}$cm/GeV^2, $F=4.42\pm0.05$, $N=4.90\pm0.06$, $m^2=0.81\pm0.04$ (GeV/c^2)^2, and $x_0=0.02\pm0.01$. The difference of the acceptances for those two distributions is considered as an uncertainty in this evaluation. We are interested in high-p_T region, $p_T\geq2.5$ GeV/c. We will present the cross sections for π^0 production in this region in Section 6.

4.3 Systematic Uncertainties in Cross Section

Systematic errors in the cross section for π^0 production have been evaluated and listed in Table 10. The p_T-independent and p_T-dependent uncertainties are shown separately. Major p_T-independent uncertainty is in the integrated luminosity. This uncertainty is evaluated from the run-to-run variation of the cross section for π^0 production in the lowest-p_T bin, which provides the highest statistics, hence the smallest statistical errors. The uncertainty has been evaluated to be 12%.

The p_T-dependent uncertainty is dominated by the reconstruction efficiency. This uncertainty is large at high p_T. The uncertainty in the geometrical acceptance is small at high p_T.

The uncertainty of p_T value is dominated by the uncertainty of energy and the position. The energy uncertainties have been estimated using the mass of π^0, η, and J/ψ. Figure 37 shows the ratio of the centroids of the mass spectra obtained by the present experiment to the values in the particle data full listing [46]. The figure

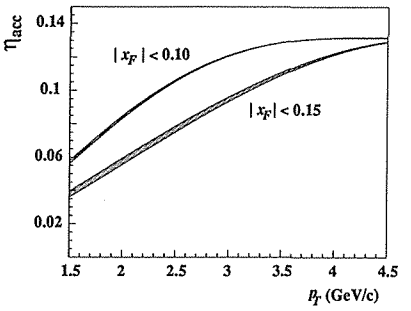

Fig. 36. Geometrical acceptances for π^0 detection in $|x_F|<0.1$ and $|x_F|<0.15$ as a function of p_T.

Table 10. Systematic uncertainties in the cross section for π^0 production.

p_T-independent uncertainties	
integrated luminosity	12%
subtotal	12%
p_T-dependent uncertainties	
reconstruction efficiencies	5-20%
geometrical acceptance	1-4%
subtotal	9-21%
uncertainties of p_T value	
incident angle of beam	$< 0.01\%$
energy-scale uncertainty	$< 0.2\%$
position uncertainties	$< 0.2\%$
subtotal	$< 0.4\%$

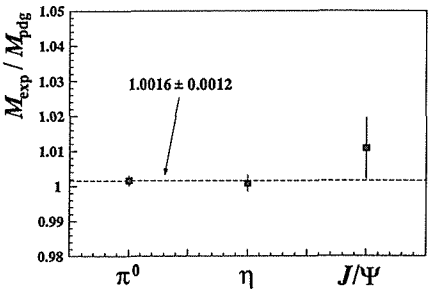

Fig. 37. Ratio of the measured mass centroids (M_{exp}) to the values from the particle data group (M_{pdg}) [46]. The dashed line represents the result of the fit to a constant value.

demonstrates the validity of the energy scale within 0.2%. The position uncertainty has been estimated from the accuracy of alignment, which has been less than 1.0 mm. It corresponds to 0.2% at the innermost column of the CEMC. The uncertainty due to the angle of the incident beam is negligible.

5 Direct-Photon Production

In this section, we describe how the direct-photon candidates have been selected and how the efficiencies of the event selection with our criteria have been evaluated. We have applied different selection criteria for obtaining the cross section and the asymmetry.

5.1 Event Selection for Deduction of Cross Section

Direct photons are expected to be more *isolated* from otherparticles than π^0's are, because π^0's are accompanied by additional particles due to the fragmentation of jet.

The application of the *isolation* criterion is efficient in discriminating direct-photon events against π^0/η events, which are major background sources. The principle of the event selection of the direct photon is (i) to select the events which occur in the target, (ii) to ensure that only one photon enters into the calorimeter, (iii) to discriminate against hadrons,(iv) to confirm that the shower in the calorimeter does not originate from the electron, (v) to assure the photon of interest is isolated from other photons. We refer to this method as *singleness* method, because the method requires only a *single* photon in the fiducial area of the CEMC and the guard counter.

The *singleness* method has dual roles; one is to reject events in which one photon from the π^0/η decay misses the CEMC by detecting the photon with the guard counter (*function of veto*). The other is to require the photon to be isolated from the ones which originate in other photon sources (*function of isolation*). The direct photons which are accompanied by π^0/η are rejected. This method is still advantageous because smaller multiplicity is expected in direct-photon events. The effect of possible over-killing of the direct-photon events is estimated later.

The criteria which correspond to the principle of the event selection are described below.

Criterion (i) The event has the reaction vertex in the target.

We have used the region $|z| \leq 56$cm taking account of the vertex resolution of z-direction which has been $\Delta z = 2.3$ cm, though the length of the target is 100 cm (see Figure 38). The vertex finding efficiency has been $33 \pm 3\%$.

Criterion (ii) The shower is not accompanied by another shower in the CEMC of the same side, i.e. *single*.

We have obtained 2,035 showers which have satisfied Criterion (i) and Criterion (ii). They have consisted of real and fake direct photons, hadrons, and electrons.

Criterion (iii) The residual ρ for shower reconstruction is less than 0.3 GeV.

The efficiency of this cut has been 95% as mentioned in the previous section. This cut has discriminated the photon from hadrons. The contamination by hadrons is evaluated to be less than 0.1% as mentioned in Section 2. The number of showers has been reduced to 1,551, whose contents have been real and fake direct photons, hadron contaminations, and electrons with this cut.

Criterion (iv) The shower is distant from the position pointed by a charge track on the surface of the CEMC by more than 20 mm.

Figure 39 shows the r^2 distribution[8] of the charged tracks where r denotes the distance between the shower position and the position of charged tracks. The figure

8 The phase space between r and $r+dr$ yields $2\pi r dr$, which is proportional to $d(r^2)$.

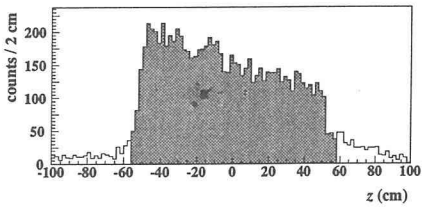

Fig. 38. The vertex distribution in z-direction. Events in the hatched area have been used for the analysis.

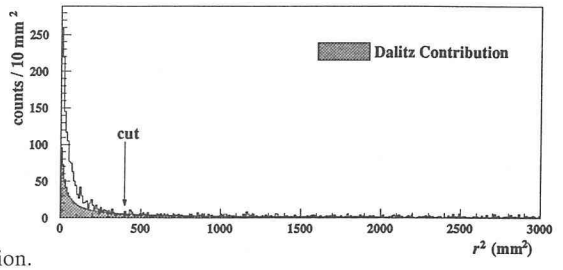

Fig. 39. The r^2 distribution of charged-particle tracks reconstructed by the MWPC's around the reconstructed shower positions. The contribution from the Dalitz decays of π^0 is indicated by the hatched area.

is made for the showers which participate to form an invariant mass of π^0. Some of those showers originated from the Dalitz decay of the π^0, and others originated from the conversion of the photon in the target materials. The conversion rate is evaluated in the next section. The cut value, $r > 20$ mm, has been determined to minimize the contamination with electrons from the Dalitz decay. This cut has reduced also the number of charged hadrons which have not been rejected by the residual cut. The number of showers has been reduced to 1,534, which have contained direct photons, fake photons, with the contamination with hadrons and electrons.

Criterion (v) The shower is not accompanied by a photon-like hit in the guard counter.

The definition of the photon-like hit is given in Section 3. This criterion is the extension of Criterion (ii), which is a requirement of the *singleness* in the CEMC, to the *singleness* in the area including the guard counter. The number of events have been reduced to 488 by this requirement.

5.1.1 Background Evaluation

As mentioned in the previous section, the *singleness* method has dual roles; one is the *function of veto* and the other is the *function of isolation*. To evaluate the background contribution after the application of the *singleness* method, we have performed a Monte Carlo simulation based on the experimental data. The motivation to use experimental data is to exclude any model dependence.

To investigate the *function of veto*, we must know the p_T distribution of the leading π^0/η and hadrons, which have the highest p_T among the produced particles. To simulate the effect of the *function of isolation*, we need to know the multiplicity and the distribution of the remnant-photon sources, which are presumably π^0's other than the leading particle. We have used the yield of the π^0/η obtained in this experiment as the p_T distribution of those leading particles. The distribution of the remnant-photon sources has been deduced from the experimental data obtained at the CERN-ISR [47].

Distribution of Photon Sources

The distribution of the remnant π^0's has been obtained from the remnant charged particle distribution measured at the CERN-ISR [47]. They measured the p_T of photons of any origin and the pseudo-rapidity distribution of charged particles in pp collisions at $\sqrt{s} = 23$ GeV,using charged-particle detectors which covered two hemispheres separately. A lead-glass calorimeter was installed in one of the hemispheres (toward side) and no calorimeter in the other one (away side). The pseudo-rapidity distribution of charged particles associated with the high-p_T photons of any origin was measured separately for the toward side and the away side. Figure 40 shows the distributions for different p_T regions of the photons.

To obtain the remnant-π^0 distribution from their charged particle distributions, we have used the compilation of the data on multiplicities of charged particles such as π, $K^{\pm}$, and $\bar{p}$ [48] in the $\sqrt{s}$ range from 3 GeV to 53 GeV. They fitted the multiplicities (n_i) to the formula

$$n_i = A_i + B_i \cdot lns + C_i\sqrt{s} \tag{27}$$

The label i indicates the particle species, π , $K^{\pm}$, or $\bar{p}$. It represents also all the charged particles. Here A_i, B_i, and C_i are the fitting parameters. The results of fitting are summarized in Table

We have calculated the ratio of the π^0 multiplicity, n_{π^0}, to the total charged particle multiplicity assuming that

$$n_{\pi^0} = \frac{1}{2}(n_{\pi^+} + n_{\pi^-}). \tag{28}$$

As a result, we have found the ratio as 0.40 ± 0.04 at $\sqrt{s} = 19.4$ GeV, the center-of-mass energy of pp collisions at 200 GeV/c. We have found also that the ratio of the charge multiplicity at 19.4 GeV to that at 23 GeV, the center-of-mass energy of the ISR data, is 0.93 ± 0.05. We have scaled the pseudo-rapidity distribution at 23 GeV multiplying by 0.93 ± 0.05 and 0.40 ± 0.04 to obtain the remnant-π^0 distribution at

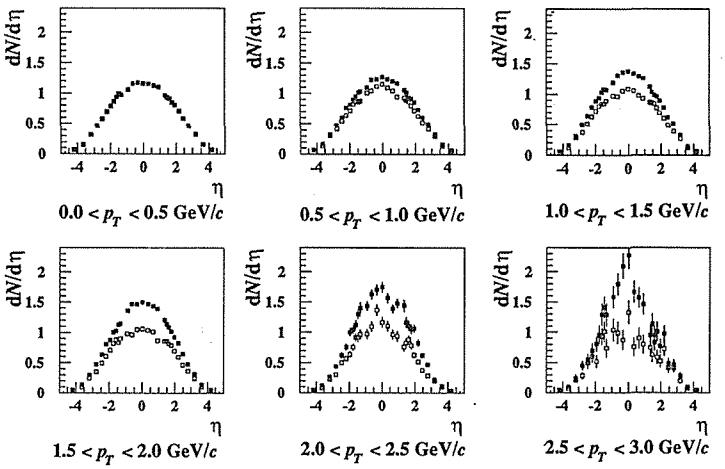

Fig. 40. Pseudo-rapidity distribution of charged particles triggeredby the detection of high-p_T photons for the toward side (open square) and for the away side (closed square). The figures are from Reference [47]

Table 11. Results of fitting of the multiplicity data to the formula (27) from [48].

type	A	B	C	χ^2/n.d.f.
n_{π^+}	-1.55 ± 0.32	0.82 ± 0.07	0.79 ± 0.47	0.5
n_{π^-}	-2.98 ± 0.22	0.94 ± 0.05	3.31 ± 0.33	0.3
n_{K^+}	-0.46 ± 0.03	0.120 ± 0.008	0.59 ± 0.05	1.5
n_{K^-}	-0.45 ± 0.03	0.100 ± 0.007	0.70 ± 0.06	1.3
n_p	-0.20 ± 0.02	0.039 ± 0.003	0.37 ± 0.04	3.6
n_{charge}	-4.32 ± 0.22	1.96 ± 0.04	7.65 ± 0.41	2.6

$\sqrt{s} = 19.4$ GeV. The total multiplicity of π^0 in the toward side is found to be 1.76 ± 0.32.

Fake Photons from π^0/η

Three types of fake events which originated from π^0/η events have been considered.

(a) two photons from the π^0 decay merge into one shower

(b) one photon from the π^0/η decay is not detected in the CEMC because the energy of the photon is below the threshold value, 0.5 GeV

(c) one photon from the π^0/η decay misses the CEMCand the guard counter.

The amount of such fake events has been estimated by means of the Monte Carlo simulation using the leading-π^0 distribution of our experimental data and the remnant-π^0 distribution obtained above. The fake event of type (c) has been evaluated from the purely geometrical acceptances of the CEMC and the guard counter. The estimations of types (a) and (b) have required the performance of the shower reconstruction. We have included the separation efficiency as a function of the distance of the two photons on the surface of the CEMC to evaluate the number of events of type (a). The energy resolution, energy threshold, and the position shift are included in the estimation of the number of events of type (b). It should be noted that the inclusion of those effects reproduces the π^0 reconstruction efficiency presented in the previous section. It has been found that the number of fake events has been reduced to $43 \pm 7\%$ due to the *function of isolation* of the *singleness* method.

The simulation has resulted in the number of the fake photons from π^0/η to be 220 ± 22.

We have performed another Monte Carlo simulation using the simulation packages of PYTHIA 5.4 and GEANT 3.15 for the evaluation of the fake events. The results of the simulation has been found to be consistent with the simulation based on the experimental data.

Contamination with Hadrons

The number of hadrons, $N_{HC}(p_T)$, which have been misidentified as the photons is written as follows:

$$N_{HC}(p_T) = \int_{q_T > p_T} (1 - \varepsilon^H_{rej})\ \zeta\ (q_T, p_T)\ N_H\ (q_T)\ dq_T. \tag{29}$$

Here ε^H_{rej} stands for the rejection efficiency for hadrons. The $\zeta\ (q_T, p_T)$ is the

response function of the CEMC for hadrons, which is defined as the probability to misidentify a hadron with the transverse momentum of q_T as a photon with the transverse momentum of p_T. The function must be zero in the region $p_T > q_T$. The $N_H(q_T)$ stands for the number of hadrons with the transverse momenta between π^0 and $q_T + dq_T$.

The $N_H(q_T)$ has been calculated to be the number of π^0 with p_T divided by 0.40 ± 0.04, which was obtained from the ISR-data mentioned in the previous section. As mentioned in the previous section (p. 12), our calibration data show

$$(1 - \varepsilon^H_{rej})\ \zeta(q_T, p_T) = 0.001, \tag{30}$$

when p_T is equal to q_T. If we assume that the response function, $\zeta(q_T, p_T)$, is independent of q_T and p_T in our regions of q_T and p_T, we could calculate $N_{HC}(p_T)$ in Equation (29) easily. Consequently, the hadron contamination has been estimated to be 49.7 ± 3.4 events. A part of them have been thrown out by the charged particle rejection in Criterion (iv). It has been expected to be 15.8 ± 1.8 events. Since the number of the showers which have been thrown out using Criterion (iv), that is 17, is consistent with this number of events, the electron contamination has been expected to be negligible. The number of rest of hadrons, 33.9 ± 3.8 events, has been reduced to 14.6 ± 2.9 by means of the "*function of isolation*" of the *singleness* method.

The ratio of the direct-photon candidates after the subtraction of hadron contaminations to the detected π^0 is plotted as a function of p_T in Figure 41. The shaded band shows the background with error evaluated in p.467 The width of the band showsthe error of the evaluation. The error bars indicate the statistical uncertainties.

5.1.2 Efficiency of Direct-Photon Detection

The evaluation of the efficiency of the *singleness* method is described in this section.

Some fraction of the direct-photon events have been rejected by the *singleness* method. For example, if a π^0 is emitted close to the direction of a direct photon, one of the decay photons from the π^0 may hit the guard counter. Such a direct-photon event might be killed by Criterion (v). In order to study such an effect, we have studied the charged particle distribution for the event when the direct photon has been produced.

We have measured the azimuthal distribution of the charged particles using the guard counter and the MWPC's. We define $\Delta\phi$ as the azimuthal opening angle between the triggered photon and the charged particle. Let F_i ($\Delta\phi$) be the $\Delta\phi$ distribution of the charged particle as

$$F_i(\Delta\phi) = \frac{1}{N_i}\frac{dN_i}{d\Delta\phi}. \tag{31}$$

Here N_i represents the number of events such as direct-photon events (N_γ), direct-photon candidates ($N_{\text{"}\gamma\text{"}}$), or π^0 and η events ($N_{\pi^0,\eta}$). The $\Delta\phi$ distribution of the charged particle for the events with the direct-photon candidate, $F_{\text{"}\gamma\text{"}}$ ($\Delta\phi$), is expressed as

$$N_{\text{“}\gamma\text{”}} F_{\text{“}\gamma\text{”}} (\Delta\phi) = N_{\pi^0,\eta} F_{\pi^0,\eta} (\Delta\phi) + N_\gamma F_\gamma (\Delta\phi). \quad (32)$$

Here the number of direct-photon candidates is denoted by $N_{\text{“}\gamma\text{”}}$. The background contribution from the π^0 and η events are represented by $N_{\pi^0,\eta}$. We have obtained the numbers, $N_{\text{“}\gamma\text{”}}$, $N_{\pi^0,\eta}$, and N_γ in the previous section to be 473 ± 3, 220±22, and 253±22, respectively. The distributions $F_{\text{“}\gamma\text{”}} (\Delta\phi)$ and $F_{\pi^0,\eta} (\Delta\phi)$ have been measured. The charged particle distribution for the direct-photon events, $F_\gamma (\Delta\phi)$, has been derived using Equation (32) with these values.

Figure 42(a) shows $N_\gamma \cdot F_\gamma (\Delta\phi)$ (closed square) and $N_{\pi^0,\eta} \cdot F_{\pi^0,\eta} (\Delta\phi)$ (open square). The histogram shows the distribution for direct-photon events

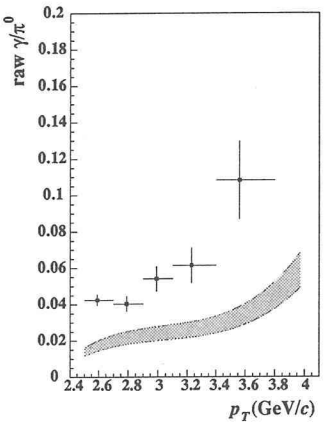

Fig. 41. Ratio of the number of direct-photon candidates to the number of π^0 as a function of p_T. The error bars indicate the statistical errors. The shaded band shows the evaluated background with error (band width) evaluated using simulations.

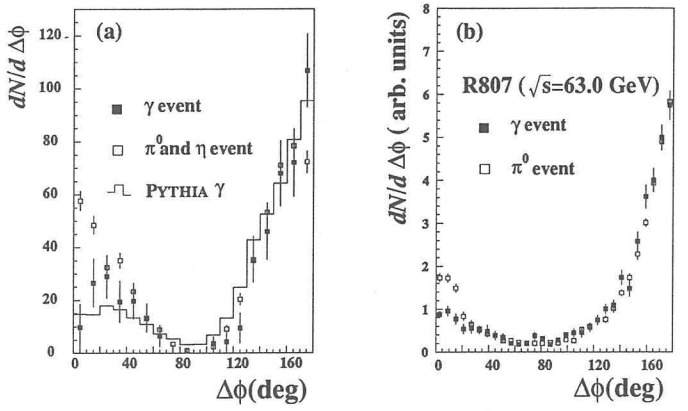

Fig. 42. $\Delta\phi$ distributions of charged particles in direct-photon events (closed square) and in π^0 events (open square) from this experiment are shown in (a) and those from R807 [11] are shown in (b). Here $\Delta\phi$ is defined as the azimuthal opening angle between the triggered photon and the charged particle. The histogram in (a) shows the distribution obtained with PYTHIA simulation.

simulated using PYTHIA 5.7[9]. The total number of $N_\gamma \cdot F_\gamma$ ($\Delta\phi$) in the region $120° \leq \Delta\phi \leq 180°$ has been normalized to that of $N_{\pi^0,\eta} \cdot F_{\pi^0,\eta}$ ($\Delta\phi$) assuming that the event structure in the away side is the same for the direct-photon events and the π^0 and η events. The less counts in the region around $\Delta\phi = 90°$ are due to the detector acceptance. Small multiplicity of charged particles around the triggered photon has been observed in the direct-photon events in comparison with that of π^0 and η events, as we expected in Section 5.1. The distribution of the direct-photon events has been found to be very close to the one obtained by the PYTHIA simulation.

Figure 42(b) shows the charged particle distributions in pp collisions at $\sqrt{s} = 63.0$ GeV measured at the ISR [11]. The distributions show the similar tendency as ours.

Since our distribution of charged particles in direct-photon events agrees with the one from the PYTHIA simulation, we have employed the PYTHIA simulation to evaluate the efficiency of the *singleness* method. It has been found that about 30% of direct-photon events has been eliminated using this method. Figure 43 shows the efficiencies of the *singleness* method as a function of p_T of the direct photon.

5.1.3 Evaluation of Systematic Errors

The systematic uncertainties in the cross section are summarized in Table 12. The uncertainty in the integrated luminosity has been estimated from the run-to-run variation of the cross section of the lowest-p_T π^0 as in the case of the π^0 cross section. The uncertainty of the target density is negligible. The uncertainty of the vertex finding efficiency has been 10%. The uncertainty in the efficiency of *singleness* method is 3%.

Table 12. Systematic uncertainties in the cross section for direct-photon production. We have evaluated the uncertainties by taking simple sums rather than quadratic sums as shown in the column labeled "subtotal".

p_T-independent uncertainties	
integrated luminosity	12%
vertex cut efficency	10%
singleness method efficiency	3%
subtotal	25%
p_T-qependent uncertainties	
geometrical acceptance	$< 1\%$
number of π^0/η	4.1-8.8%
multiplicity of π^0	4.9-7.0%
subtotal	9.0-16%
uncertainties of p_T value	
incident angle of beam	$<0.01\%$
energy-scale uncertainty	$< 0.2\%$
position uncertainties	$< 0.2\%$
subtotal	$< 0.4\%$

[9] During this analysis, the simulation package PYTHIA has been updated, though there is no change in the reactions we have studied.

The origins of the p_T-dependent uncertainty are in the numbers of π^0 and η mesons and the multiplicities of π^0 and η mesons.

The uncertainty of p_T value has been estimated as in the same way as in the case of π^0 production.

5.2 *Event Selection for Deduction of Asymmetry*

5.2.1 *Away-Side Requirement for Direct-Photon Candidates*

Since the vertex finding efficiency is not so great, that is 33%, we have replaced the vertex cut with "*away-side cut*" which has required at least one charged or neutral particle in the region of $\cos\Delta\phi < -0.6$ on any of the CEMC, the guard counter, or the MWPC, where $\Delta\phi$ is defined as the azimuthal opening angle between the particle and the direct-photon candidate. The efficiency of this cut has been estimated with the two types of Monte Carlo simulations mentioned above. One of them has been developed on the basis of experimental data and the other one is based on the simulation packages of PYTHIA and GEANT. The developed simulation has resulted in 93% for the efficiency and the simulation with PYTHIA and GEANT has given 94%. Since the particle distribution in the away side for direct-photon events is similar to the one for the π^0 events as shown in the previous section, we expect that the efficiency for direct-photon events is the same efficiency as that of our high-p_T π^0 events, which has given $93.2 \pm 3.4\%$. This value is the same as the ones obtained with the simulations within the errors, hence it demonstrates the reliability of the simulations. The efficiency estimated using the simulation packages of PYTHIA and GEANT is plotted as a function of p_T in Figure 44.

After the selection with Criteria (ii)-(v) and the "*away-side cut*" instead of vertex cut, we have obtained 1,557 direct-photon candidates. It is worth mentioning that 98% of vertex cut events satisfies the "*away-side cut*".

In order to estimate the contamination with the events from out of the target, we have compared the p_T spectra of the photons obtained by the "*away-side cut*" with the spectrum obtained by the vertex cut. For this purpose we have decomposed the spectrum before the vertex cut into two components, one for the events with the vertex inside the target, $N^{\gamma}_{in}(p_T)$ and that with the vertex out of the target, $N^{\gamma}_{out}(p_T)$. It has been found that the slope of N^{γ}_{in} in (p_T) is steeper than that of $N^{\gamma}_{out}(p_T)$. Thus it

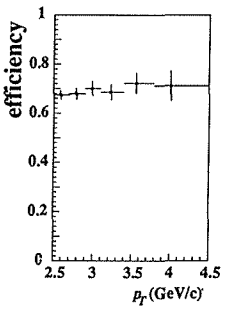

Fig. 43. Efficiency of the *singleness* method as a function of p_T.

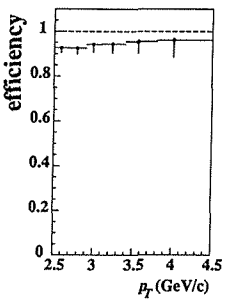

Fig. 44. Efficiencies of *away-side cut* method as a function of p_T.

it possible for the spectrum obtained by the "*away-side*" cut, $N^{\gamma}_{away}(p_T)$, to be fit to the equation

$$N^{\gamma}_{away}(p_T) = \alpha N^{\gamma}_{in}(p_T) + \beta N^{\gamma}_{out}(p_T). \tag{33}$$

We have obtained the results as

$$\begin{cases} \alpha = 2.90 \pm 0.20, \\ \beta = 0.15 + 0.08, \end{cases}$$

where the reduced χ^2 is 1.33. Here we expect the value of α as,

$$\alpha = \frac{\varepsilon_{away}}{\varepsilon_{vertex}}, \tag{34}$$

which has been calculated to be 2.85 with the values of $\varepsilon_{away}=0.94$ and $\varepsilon_{vertex}=0.33$. Hence the results of the fit are consistent with our expectation. The estimated background contribution is shown in Figure 45. The ratio of the background to the total events ranges from 6.4 to 8.7% in the region, $2.5 \leq p_T \leq 3.1$ GeV/c. We have used this region to derive the asymmetry A_N. Averaging over the p_T region, we have evaluated the contamination to be $7.4 \pm 0.7\%$.

5.2.2 Determination of Asymmetry and Systematic Uncertainties

The asymmetry A_N is calculated as,

$$A_N = \frac{1}{P_B} \frac{\sigma(L) - \sigma(R)}{\sigma(L) + \sigma(R)}. \tag{35}$$

Here P_B denotes the average beam polarization, which has been $46\% \pm 1.9\%$. The $\sigma(L)$ and $\sigma(R)$ represent the cross sectionsfor the direct-photon productions in "left" and "right" sides, respectively. The "left" side is defined as the left side seen from upstream when the beam polarization is "up". The rotational symmetry around the beam axis requires that the cross section for the "left" by "up" is equal tothat for the "right" by "down". Hence we have calculated $\sigma(L)$ and $\sigma(R)$ as

$$\sigma(L) = \frac{1}{2}\{\sigma(\uparrow,1) + \sigma(\downarrow,2)\} \tag{36}$$

$$\sigma(R) = \frac{1}{2}\{\sigma(\downarrow,1) + \sigma(\uparrow,2)\} \tag{37}$$

Here $\sigma(\uparrow,i)$ and $\sigma(\downarrow,i)$ denote the cross sections obtained with the beams polarized

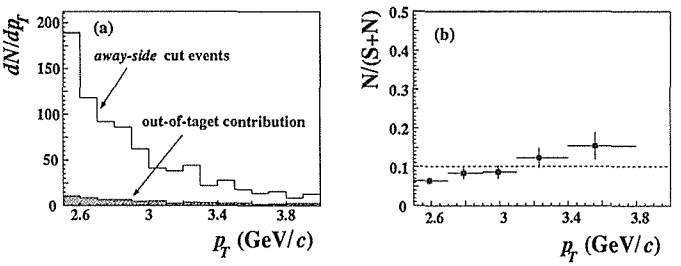

Fig. 45. (a)Background contribution to the events selected with *away-side cut* as a function of p_T. (b)Ratio of the number of the estimated background to the number of total events as a function of p_T. The error bars indicate statistical errors.

in "up" and "down" directions, respectively, using the the CEMCi (i=1,2).

Possible origins of fake asymmetry are in the beam counting, and the difference in the detection efficiency between CEMC1 and CEMC2. To estimate how those effects contribute to the asymmetry, let us suppose that the beam counting causes the cross section asymmetry (α_B) as

$$\frac{\bar{\sigma}(\downarrow)}{\bar{\sigma}(\uparrow)} = 1 + \alpha_B. \tag{38}$$

Here $\bar{\sigma}$ denotes the experimentally determined cross section which is different from the real valuedue to a possible problem in beam counting. Let us suppose that the difference in the detector responses causes the cross section asymmetry (α_D) as

$$\frac{\bar{\sigma}(2)}{\bar{\sigma}(1)} = 1 + \alpha_D. \tag{39}$$

Then the experimentally determined asymmetry, $\widehat{A_N}$, will be,

$$\widehat{A_N} = \frac{1}{P_B}\frac{\bar{\sigma}(\uparrow,1)+\bar{\sigma}(\downarrow,2)-\bar{\sigma}(\uparrow,2)-\bar{\sigma}(\downarrow,1)}{\bar{\sigma}(\uparrow,1)+\bar{\sigma}(\downarrow,2)+\bar{\sigma}(\uparrow,2)+\bar{\sigma}(\downarrow,1)}$$

$$= \frac{1}{P_B}\frac{\sigma(\uparrow,1)+(1+\alpha_D)(1+\alpha_B)\sigma(\downarrow,2)-(1+\alpha_D)\sigma(\uparrow,2)-(1+\alpha_B)\sigma(\downarrow,1)}{\sigma(\uparrow,1)+(1+\alpha_D)(1+\alpha_B)\sigma(\downarrow,2)+(1+\alpha_D)\sigma(\uparrow,2)+(1+\alpha_B)\sigma(\downarrow,1)}$$

Here we have converted the experimental cross sections ($\bar{\sigma}$) to real ones (σ) using the asymmetry parameters, α_B and α_D. The rotational symmetry requires real cross sections to be

$$\sigma(\uparrow,1) = \sigma(\downarrow,2) = \sigma(L) \tag{40}$$

$$\sigma(\uparrow,1) = \sigma(\downarrow,2) = \sigma(R) \tag{41}$$

Hence the experimentally determined asymmetry $\widehat{A_N}$ is,

$$\widehat{A_N} = \frac{1}{P_B}\frac{(1+1+\alpha_D+\alpha_B+\alpha_D\alpha_B)\sigma(L)-(1+\alpha_D+1+\alpha_B)\sigma(R)}{(1+1+\alpha_D+\alpha_B+\alpha_D\alpha_B)\sigma(L)+(1+\alpha_D+1+\alpha_B)\sigma(R)} \tag{42}$$

If we assume that $\alpha_B \ll 1$ and $\alpha_D \ll 1$, we can neglect $\alpha_B \cdot \alpha_D$ comparing to unity. Then the asymmetry will be,

$$\widehat{A_N} = A_N. \tag{43}$$

Since the asymmetry α_B is solely relevant to the beam, the α_B has been estimated using the cross section for the π^0 production, which has much higher statistics than that ofthe direct-photon production.

$$1+\alpha_B = \frac{\sigma^{\pi^0}(\downarrow,1)+\sigma^{\pi^0}(\downarrow,2)}{\sigma^{\pi^0}(\uparrow,1)+\sigma^{\pi^0}(\uparrow,2)}. \tag{44}$$

The result shows $\alpha_\beta = -5 \pm 2\%$.

For the evaluation of the asymmetry α_D, we have used all the beam phase space, including unpolarized part of the beam. As the asymmetry might depend on the particle and on its p_T, the asymmetry has been estimated for only the direct-photon candidates in the p_T region of interest, $2.5 \leq p_T \leq 3.1$ GeV/c.

$$1+\alpha_D = \frac{\sigma^\gamma(\uparrow,2)+\sigma^\gamma(\downarrow,2)+\sigma^\gamma(0,2)}{\sigma^\gamma(\uparrow,1)+\sigma^\gamma(\downarrow,1)+\sigma^\gamma(0,1)} \tag{45}$$

Here $\sigma^\gamma(0,1)$ and $\sigma^\gamma(0,2)$ denote the cross sections obtained using unpolarized part of the beam with CEMC1 and CEMC2, respectively. The result shows α_D =

$7.4 \pm 13.3\%$. Hence it has been found that $\alpha_B \cdot \alpha_D = -0.37 \pm 0.68\%$. False asymmetry, $\overline{A_N}$, due to those asymmetries has been evaluated as

$$\overline{A_N} = \frac{1}{P_B} \frac{(1+1+\alpha_D+\alpha_B+\alpha_D\alpha_B) - (1+\alpha_D+1+\alpha_B)}{(1+1+\alpha_D+\alpha_B+\alpha_D\alpha_B) + (1+\alpha_D+1+\alpha_B)} = 0.002. \quad (46)$$

The asymmetry is affected by the uncertainty in the absolute beam polarization, which has been $46 \pm 1.9\%$, which corresponds to the uncertainty of 4.1% for A_N. The background in the *away-side cut* also affects the asymmetry. The contribution of this background in the p_T range of interest has been $7.4 \pm 0.7\%$. The uncertainty has been estimated to be 16%.

The uncertainty of p_T value has been estimated in the same way as in the case of the cross section for the π^0 production.

The uncertainties in the asymmetry are tabulated in Table 13.

6 Results and Discussion

6.1 Cross Section for π^0 Production

The invariant cross section for inclusive π^0 production in $|x_F| < 0.1$ has been obtained as a function of p_T. The results are tabulated in Table 14. The first error represents the statistical one and the second error represents the systematic one. The systematic uncertainty in the high-p_T region mainly originates from the evaluation of the reconstruction efficiency. The data are shown in Figure 46. Plotted together are the cross sections measured at FNAL using a 200-GeV/c proton beam upon a liquid-hydrogen target (open square) [49]. The dashed lines show the results of the global fit of the ISR data in $23.5 < \sqrt{s} < 62.4$ GeV [50]. The curves are extrapolated to 19.4 GeV. The difference between two lines reflects the errors in fitting parameters. The solid line shows the fit of the FNAL data, in which $\sqrt{s}$ ranges from 13.7 GeV to 23.8 GeV [45].

Good agreement among the experimental data has been found. Although the

Table 13. Systematic uncertainties in asymmetry A_N. The subtotal of the uncertainty in the absolute values has been calculated by Equation (46).

absolute values of asymmetry	
beam asymmetry	5%
detector asymmetry	7.4%
subtotal(false asymmetry)	0.20%
scale of asymmetry	
absolute polarization	4.1%
background in *away-side* cut	16%
subtotal	20%
uncertainties in p_T value	
incident angle of beam	$< 0.01\%$
energy-scale uncertainty	$< 0.2\%$
position uncertainties	$< 0.2\%$
subtotal	$< 0.4\%$

Table 14. Invariant cross sections for π^0 production in $|x_F| < 0.01$ in pp collisions at 200 GeV/c. The p_T in the second column shows the average transverse momentum. The first errors of the cross sections are of statistical ones and the second errors are systematic ones.

p_T range(GeV/c)	p_T(GeV/c)	$E\frac{d^3\sigma}{dp^3}$(cm^{2}GeV$^{-2}c^3$)
2.5-2.7	2.59	$(1.84 \pm 0.02 \pm 0.11) \times 10^{-31}$
2.7-2.9	2.79	$(8.08 \pm 0.13 \pm 0.49) \times 10^{-32}$
2.9-3.1	2.99	$(3.63 \pm 0.08 \pm 0.21) \times 10^{-32}$
3.1-3.4	3.23	$(1.42 \pm 0.04 \pm 0.08) \times 10^{-32}$
3.4-3.8	3.56	$(3.77 \pm 0.39 \pm 0.28) \times 10^{-33}$
3.8-4.5	4.06	$(7.14 \pm 0.75 \pm 1.47) \times 10^{-34}$

fitting curves disagree each other in lower-p_T region, they agree with our data in our p_T region. Therefore, the cross section for production of high-p_T π^0 in pp collisions is well understood in the kinematical region of interest, $2.5 < p_T < 4.5$ GeV/c at $\sqrt{s} = 19.4$ GeV.

6.2 Cross Section for Direct-Photon Production

Results

The direct-photon candidates have been deduced in the previous section. According to Monte Carlo simulations, the signal-to-noise ratio has been improved to about 1:1 for the sake of the *singleness* method. And about a half of the candidates has been found to be the background from π^0/η. Other contaminations such as electrons and hadrons have been negligible. Those backgrounds have been subtracted statistically. The efficiency of our analysis has been evaluated using Monte Carlo simulations.

The cross section for inclusive direct-photon production in $|x_F| < 0.15$ in pp collisions at 200 GeV/c has been obtained by correcting the yield of direct photons by detection efficiencies. Results are tabulated in Table 15. The first errors are statistical ones and the second errors are the systematic ones. Normalization uncertainty has been evaluated to be 25%.

The data are plotted in Figure 47 together with the cross section per nucleon measured in previous experiments using carbon targets at CERN [14] and at Fermilab [15]. The error bars indicate the statistical ones. The dashed curve shows the result of phenomenological fit in Reference [15]. The previous experimental data agree with our data within experimental uncertainties, if we assume that the cross section is proportional to the atomic number.

The solid and dashed lines show theoretical calculations by Owens [51] and by Aurenche *et al.* [5] using the sets of structure functions, that is Duke-Owens (DO) set 1 (dashed lines) and set 2 (solid lines) [52]. The cross sections were calculated for the p_T region above some p_T threshold. The threshold corresponded to lower limit of Q^2 to apply the structure functions, that is 4 GeV^2. These calculations were made up

to next-to-leading order including the bremsstrahlung contribution to direct photons. The data seem to favor the structure function DO set 2, which has harder gluon distribution than DO set 1.

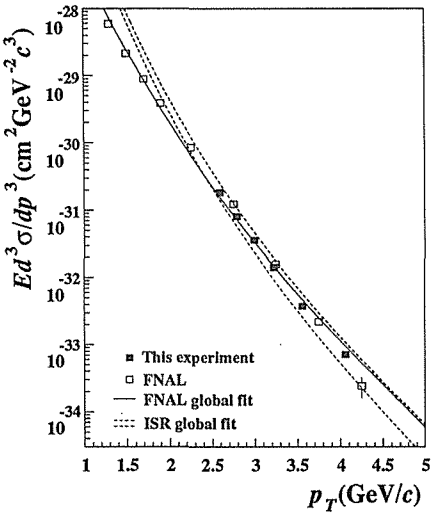

Fig. 46. Invariant cross section for the π^0 production in $|x_F| < 0.10$ in pp collisions at 200 GeV/c as a function of p_T. The data from previous measurements are also plotted. The solid curveshows results of phenomenological fit in Reference [45]. The dashed lines are fit of the ISR data to an empirical form, where the $\sqrt{s}$ ranges from 23.5 GeV to 62.4 GeV.

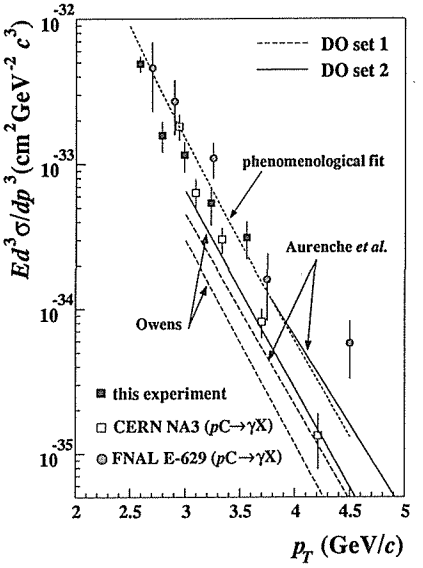

Fig. 47. Invariant cross section for direct-photon production in $|x_F| < 0.15$ in pp collisions at 200 GeV/c as a function of p_T. The data from previous measurements at CERN [14] and at Fermilab [15] are also plotted. Dotted curveshows the results of phenomenological fit in Reference [15]. Theoretical calculations by Owens [51] and by Aurenche *et al.* [5] using the structure function of Duke-Owens (DO) set 1 (dashed lines) and set 2 (solid lines) are also shown.

Table 15. Invariant cross sections for direct-photon production in pp collision at 200 GeV/c. The p_T shows the average transverse momentum. The first errors of cross sections are of statistical nature, while the second ones represent the systematic uncertaintes. Normalization uncertainty is evaluated to be 25%.

p_T range(GeV/c)	p_T(GeV/c)	$E\frac{d^3\sigma}{dp^3}$(cm^{2}GeV$^{-2}c^3$)
2.5-2.7	2.59	$(4.90 \pm 0.61 \pm 0.49) \times 10^{-33}$
2.7-2.9	2.79	$(1.58 \pm 0.38 \pm 0.25) \times 10^{-33}$
2.9-3.1	2.99	$(1.15 \pm 0.27 \pm 0.13) \times 10^{-33}$
3.1-3.4	3.23	$(5.39 \pm 1.60 \pm 0.59) \times 10^{-34}$
3.4-3.8	3.56	$(3.12 \pm 0.91 \pm 0.27) \times 10^{-34}$

Phenomenological Analysis

Figure 48 shows the invariant cross sections for inclusive direct-photon production in pp collisions in the range 19.4 GeV $< \sqrt{s} <$ 63.0 GeV. The data from E629 and NA3 were obtained using a carbon target, and the data from E706 were obtained using a beryllium target. Therefore, the data are normalized by the atomic numbers. The curves are the global-fit[10] to the form

$$E\frac{d^3\sigma}{dp^3} = \frac{A}{p_T^a}\, x_T^a\ (1-x_T)^b. \tag{47}$$

Here x_T is defined as

$$x_T = \frac{2p_T}{\sqrt{s}}. \tag{48}$$

The values of fitting parameters are summarized in Table 16. To demonstrate the x_T-scaling behavior of the cross section, which presumably reflects the Bjorken scaling, the data on $p_T^n \cdot E\frac{d^3\sigma}{dp^3}$ are shown in Figure 49. In order to examine whether the expression (47) holds for a very large $\sqrt{s}$ range, we have performed two additional fits; one of them has been performed without the data at the lowest $\sqrt{s}$ (19.4 GeV) among the data set and the other is done without the ones at the highest $\sqrt{s}$ (63.0 GeV). These fits give χ^2 per degree of freedom around unity, but contributions

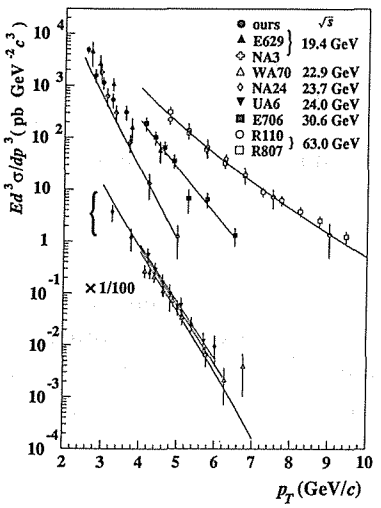

Fig. 48. Cross sections for direct-photon production in pp collisions in 19.4 $< \sqrt{s} <$ 63.0 GeV. In this figure, the cross sections for 22.9 $< \sqrt{s} <$ 24.0 GeV are divided by 100. The solid curves show the results of the fit to the Equation (47) at each $\sqrt{s}$. Smaller cross section corresponds to smaller $\sqrt{s}$.

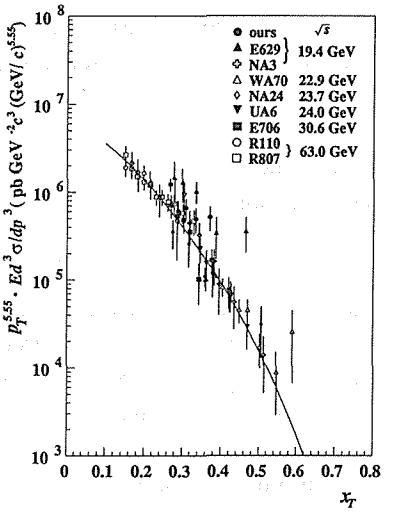

Fig. 49. x_T-dependence of the cross sections for direct-photon production in pp collisions in 19.4 $< \sqrt{s} <$ 63.0 GeV. Solid curveshows the result of the fit to the Equation (47).

[10] It is pointed out that the formula is not expected to hold in very large p_T and $\sqrt{s}$ region [53].

Table 16. Results of phenomenological fits of the data to Equation (47). The fit I has been done with all the data. The fit II has been performed without the data of the lowest $\sqrt{s}$ (19.4 GeV), while the fit III has been done without the data of the highest $\sqrt{s}$ (63.0 GeV).

fit	A	n	a	b	X^2/ndf
I	6.69×10^6	5.55	0.01	9.18	61.2/61
II	2.63×10^6	5.36	− 0.25	8.44	20.4/45
III	1.46×10^5	6.79	− 2.81	3.14	46.5/43

of 19.4-GeV data to the χ^2 are significant as seen from Table 16. This fact suggests the existence of another source of the direct photon in lower-$\sqrt{s}$ region, such as the bremsstrahlung from final state particles.

Comparison with LUND-model Calculations

The PYTHIA is a simulation package which generates events of hard processes in the leading order utilizing the LUND fragmentation model [43] for the subsequent fragmentation of quarks and gluons into hadrons and photons. To extract realistic numerical values from the PYTHIA simulation, we must tune several parameters; the K-factor, the choice of structure functions, k_T smearing, and Q^2 definition. Brief discussions on these parameters are given in order.

Even though the simulation includes only leading order processes, effects of higher order processes can be included through the K-factor. Here the K-factor is defined as the ratio of the full summation of perturbation series of the cross section to the cross section in the leading order (σ_0) as,

$$\sigma_0 + \alpha_s\sigma_1 + \cdots = K \cdot \sigma_0. \tag{49}$$

In the PYTHIA, the K-factor is introduced effectively through a shift of the Q^2 in $\alpha_s\,(Q^2)$ as $\alpha_s\,(0.075Q^2)$. The effective K-factor thus obtained is in accordance with the results in Reference [54]. For example, the direct-photon cross section in next-to-leading order was calculated by Aurenche [5], and the K-factor was found to be approximately 2. The effective K-factor which is included in PYTHIA simulation is also about 2 in our $\sqrt{s}$ region.

In the current version of PYTHIA, the structure function set is CTEQ2L [55], if not specified. The set was the best leading order fit at the time of the release of the PYTHIA. The precision measurement of $F_2^p(x)$ by deep-inelastic scattering of muon from the proton target [56] favors GRV [57] set. The ABFOW set was obtained from the detailed analysis of the cross sections for the direct-photon production in pp and $\bar{p}p$ collisions. We have employed the GRV, ABFOW, and CTEQ2L sets for the simulation.

The k_T denotes the intrinsic transverse momentum of partons. In the parton model, the k_T reflects the size of the hadron via the uncertainty principle. The existence of k_T leads to the increase of cross section. In PYTHIA k_T is smeared to have a Gaussian distribution with σ of 0.44 GeV/c. We have employed this distribution.

There is an uncertainty in the choice of Q^2 scale, which is used to evaluate the running coupling constant and structure functions. The Q^2 is often related to p_T of the produced photon as

$$Q^2 = C \cdot p_T^2, \tag{50}$$

where C ranges from about 0.25 to 4.0. Lower value of C results in larger cross section. We have employed the value of C as 0.25 for our simulation according to the discussion in Reference [58].

The bremsstrahlung contribution isnot included in the PYTHIA simulation of the direct-photon production[11].

Figure 50 shows the comparison between the experimental results and the simulation. The simulation has been performed at four $\sqrt{s}$ points; 19.4 GeV, 22.9 GeV, 30.6 GeV, and 63.0 GeV. Four types of simulations have been done for each $\sqrt{s}$ point; the simulations in the leading order using (i) CTEQ2L (ii) ABFOW (iii) GRV set of structure functions and (iv) the simulation including the effective K-factor with CTEQ2L set. Among them, the CTEQ2L gives the largest cross section, and the GRV set gives the smallest. This is attributed to the large gluon content in the kinematical range of interest. The CTEQ2L with the effective K-factor reproduces the data well, while simulations tend to overestimate in higher-p_T region and underestimate in lower p_T region. One of the reasons of the discrepancy in lower p_T region is in the fact that the bremsstrahlung contribution is not included in the simulation. To understand the cross section more precisely, further investigation of the direct-photon production in lower p_T region is necessary. For example, the measurement of the multiplicity of charged particles in the direct-photon production will provide useful information on the production mechanism.

6.3 Asymmetry for Direct-Photon Production

The single transverse-spin asymmetry A_N for the direct-photon production in pp collision at 200 GeV/c has been obtained in the region, $2.5 < p_T < 3.1$ GeV/c and $|x_F| < 0.15$. The data are averaged over $2.5 < p_T < 3.1$ GeV/c and presented in two x_F bins, $-0.15 < x_F < 0.00$ and $0.00 < x_F < 0.15$. The averaged p_T is 2.73 GeV/c, which corresponds to $x_T = 0.28$, for both x_F bins. The background contributions are estimated separately for each x_F bins and each beam polarization, "up"($\uparrow$) and "down"($\uparrow$), using the number of π^0/η in each bin. Therefore, possible asymmetry in π^0/η productions are excluded from the direct-photon asymmetry, although the asymmetry in π^0 productions is found to be consistent with zero [59].

The obtained asymmetry is tabulated in Table 17. The first errors are of statistical nature and the second ones are systematic uncertainties. The systematic errors mainly originate from the uncertainties in the number of leading π^0/η's and the multiplicity of the remnant π^0's used for calculations of fake event contributions. There is an uncertainty in the scale of the asymmetry, which originates from the

[11] It is not impossible to include the bremsstrahlung in the PYTHIA simulation, although such a simulation invests extensive CPU time. We have included only the gluon "Compton" and annihilation subprocesses in the simulation.

Table 17. Single spin asymmetries for direct-photon production in pp collisions at 200 GeV/c. The x_F in the second column shows the average value. Asymmetries are followed by statistical errors and systematic errors. Average p_T is 2.73 GeV/c.

x_F range	x_F	$A_N(\%)$
-0.15-0.00	-0.04	16.7 ± 30.0 ± 7.4
0.00-0.15	0.06	-0.6 ± 21.6 ± 5.7

absolute beam polarization and from the out-of-target events. The scale uncertainty is estimated to be 20%.

Figure 51 shows the obtained asymmetries. The statistical errors are indicated as the error bars and the systematic uncertainties are indicated as squared brackets additively to the statistical errors. The solid and dashed curves show theoretical predictions on the asymmetry [32] using two models on the twist-3 matrix element $T(x,s_T)$,

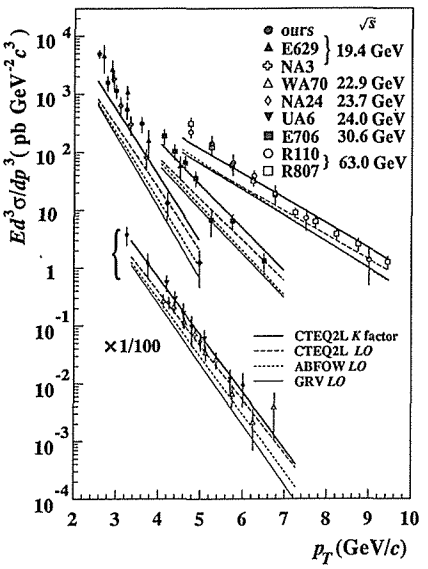

Fig. 50. Comparison of the cross sections for direct-photon production in pp collisions between the experimental data and the PYTHIA calculations with several choices on the set of structure functions, CTEQ2L, GRV, ABFOW. The lines indicated by *LO* are for the calculations in the leading order. The effective K-factor is included in the indicated lines. The Q^2 scale is assumed to be $0.25p_T^2$.

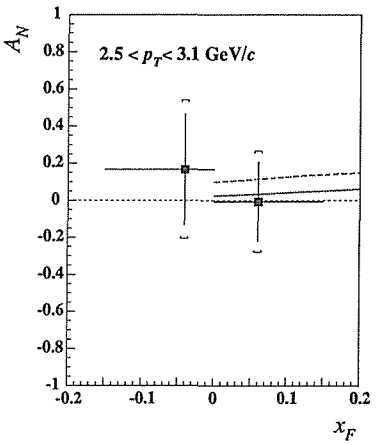

Fig. 51. Single transverse-spin asymmetry A_N for direct-photon production in pp collisions as a function of x_F. The presented data are the results obtained in $2.5 \leq p_T \leq 3.1$ GeV/c. The error bars indicate the statistical one and the squared brackets show the systematic uncertainties additively to the statistical ones. The solid and dashed curves show the predicted asymmetry by Qiu and Sterman [32] using two different models for the twist-3 matrix element shown in Equations (51) and (52), respectively.

$$T_I(x,s_T) \approx C_T \cdot F_2(x)/x \quad \text{(GeV)} \quad \text{(model)} \tag{51}$$

$$T_{II}(x,s_T) \approx C_T \cdot F_2(x) \quad \text{(GeV)} \quad \text{(modelI)} \tag{52}$$

Here they took mass scale parameter C_T as 0.2 GeV. Their calculation has actually been done for $\sqrt{s}=30$ GeV and $p_T=4.0$ GeV/c, hence $x_T=0.27$. The x_T value is similar to ours, that is $x_T=0.28$. In the direct comparison, however, one should think of several Q^2-dependent factors; one originates from the running coupling constant $\alpha_s(Q^2)$, one from the Q^2-evolution of structure functions, and $1/\sqrt{Q^2}$ dependence of the twist-3 contribution.

In spite of the difference in Q^2 scale, the data suggests that the strength of the quark-gluon correlation does not exceed their estimation.

Recently the Spin Muon Collaboration (SMC) at CERN measured the spin dependent structure function of the proton, $g_2^p(x)$ [61 – 66], using a longitudinally-polarized muon and a transversely-polarized target [67]. The function $g_2^p(x)$ consists of pure twist-3 part and the term which is related to $g_1^p(x)$. Their data are consistent with the assumption that the pure twist-3 part of $g_2^p(x)$, that is $\overline{g_2^p}(x)$, is identical to zero. According to Ehrnsperger *et al.* [68], there is a relation between twist-3 matrix element, $T(x, s_T)$, and $\overline{g_2^p}(x)$ as,

$$\int_{-1}^{1} T(x,s_T)\,dx = -12\,cM^2R_0\int_0^1 x^2\overline{g_2^p}(x)\,dx. \tag{53}$$

Here R_0 denotes the radius of the proton, c takes the value ranging from 1/3 to 1, and M stands for the mass of the proton. Our data and the SMC data, which are interpreted to exclude a large twist-3 contribution, are consistent, although both data do not provide the full integration of the functions. To determine the magnitude of the twist-3 contribution, further investigations with high statistics and larger acceptance to cover large positive and negative x_F regions are desired.

The asymmetry A_N for direct-photon production has been measured for the first time and the data have provided a limit on the quark-gluon correlation in the proton. The measurement have shed the light on the spin structureat the twist-3 level. The data also clarified that the production mechanism of the direct photon in this kinematical region must be understood in more quantitative way to elucidate the spin structure of hadrons.

7 Conclusion

The single transverse-spin asymmetry for direct-photon production has been measured for the first time using the polarized-proton beam of 200 GeV/c upon unpolarized liquid-hydrogen target at Fermilab Spin Physics Facility. The cross sections for $pp \rightarrow \gamma X$ have also been measured. The high-p_T direct-photon production in pp collisions has been considered to be sensitive to the gluon content of the proton because the production is dominated by the gluon "Compton" subprocess. In the context of the study of the spin structure of the proton, the direct photon is expected to become more important in understanding the role of gluon in the spin

polarization of the proton. The asymmetry A_N in the direct-photon production is considered to be sensitive to the spin structure of the proton at the twist-3 level, which is normally suppressed by $\frac{1}{\sqrt{Q^2}}$ with respect to the leading term. The asymmetry, however, has never been measured yet because of a lack of high-energy polarized beam and smallness of the production cross section. We have made the measurement feasible by the construction of the polarized-proton beam utilizing the Λ-decay and the installation of the finely-granulated calorimeter and the photon detector (guard counter) which has surrounded the fiducial area of the calorimeter. The photon detector has been useful to reduce the background significantly.

The extraction of the direct photon has been done on the basis of (i) background rejection using the photon detector, (ii) the precision measurement of yields of π^0 and η mesons which are the major background, and (iii) the detailed study of the event structure utilizing both of the experimental data and Monte Carlo simulations. As a consequence, the data on the cross section and the asymmetry for direct-photon production have been obtained as well as the cross section for the π^0 production.

The obtained π^0 cross sections agree to those by the previous measurements using the proton beam on liquid hydrogen target. Phenomenological fits of the ISR data in $23.5 \leq \sqrt{s} \leq 62.4$ GeV and the Fermilab data in $13.7 \leq \sqrt{s} \leq 23.8$ GeV have agreed with our data. Therefore, the cross section for π^0 productionis well understood.

The cross section for the direct-photon production has been obtained for $|x_F| < 0.15$ and $2.5 \leq p_T \leq 3.8$ GeV/c as a function of p_T. This is the first data in pure pp collisions at 200 GeV/c. The cross section for the direct-photon production agrees with the previous data obtained using the proton beam on carbon target at FNAL and at CERN, assuming that the cross section is proportional to the atomic number of the target. Theoretical calculations agree with our data. The data favors a hard gluon distribution. The data in $19.4 \leq \sqrt{s} \leq 63.0$ GeV have been successfully fit to the form $E\frac{d^3\sigma}{dp^3} = \frac{A}{p_T^n} x_T^a (1-x_T)^b$. The leading order calculations using the PYTHIA simulation underestimate the cross section. If higher-order effects are taken into account, the simulation gives a better description of the data in $19.4 \leq \sqrt{s} \leq 63.0$ GeV.

The asymmetry A_N for the direct-photon production has been measured in $|x_F| < 0.15$ and $2.5 \leq p_T \leq 3.1$ GeV/c as a function of x_F. The measured asymmetry A_N is consistent with zero within the experimental accuracy. In this sense, the data do not suggest a strong quark-gluon correlation exceeding the theoretical assumption made by Qiu and Sterman. The measurement have shed the light on the spin structure at the twist-3 level. The data have also clarified that the production mechanism of the direct-photon in this kinematical region must be investigated in more quantitatively to extract the spin structure from the data. The study will be extended to include a larger kinematical region and higher statistics and elucidate the spin structure of the nucleon. The present experimental data have provided the basis of such studies.

Acknowledgements

First of all, I would like to express my sincere and special thanks to Professor Akira Masaike who has been my supervisor. He has encouraged me since my time in undergraduate course.

I would express my gratitude to all the members of E704 collaboration. Without their great efforts, I could not complete this paper. I would thank to the staff of Fermi National Accelerator Laboratory (FNAL) for supporting the present experiment. The data summary tape has been made using the program TQBANK developed by Professor Junsei Chiba and Professor Tadayuki Takahashi and installed to our machine by Yuji Goto. I would like to thank all of them.

The present work has been stimulated by many theoreticians. I would like to thank Professor R.L. Jaffe for discussionson the structure functions at Shimoda and Brookhaven. I also thank Professor A. Efremov and Professor O. Teryaev for useful discussions at Nagoya and Bloomington. I am grateful to Professor G. Sterman for his explanation on the asymmetry for the direct-photon production. I would express a gratitude to Professor P. Aurenche for his calculation of the cross section for direct-photon production.

References

[1] E. D. Bloom *et al*, Phys. Rev. Lett. **23** (1969) 930.
[2] M. Bredenbach *et al*, Phys. Rev. Lett. **23** (1969) 935.
[3] R. P. Feynman, Phys. Rev. Lett. **23** (1969) 1415; *Photon Hadron Interactions,* W. A. Benjamin, New York(1972).
[4] For the most recent works, see A. D. Martin, W. J. Stirling, and R. G. Roberts, Phys. Rev. **D50** (1994)6734and H. L. Lai *et al.*, Michigan State University Preprint MSU-HEP-41024 (hep-ph/9410404), "Global QCD Analysis and the CTEQ Parton Distributions"
[5] P. Aurenche *et al.*, Phys. Rev. **D39** (1989) 3275.
[6] J. F. Owens, Phys. Lett. **B266** (1991) 126.
[7] A. D. Martin, R. G. Roberts, and W. J. Stirling, Phys. Rev. **D47** (1993) 867.
[8] G. Sozzi *et al.*, Phys. Lett. **B317** (1993) 243; G. Ballochi *et al.*, Phys. Lett. **B317** (1993) 250.
[9] G. Alverson *et al.*, Phys. Rev. **D48** (1993) 5.
[10] A. L. S. Angelis *et al*, Nucl. Phys. **B327** (1989) 541.
[11] T. Åkesson *et al.*, CERN-EP/89-98.
[12] M. Bonesini *et al.*, Z. Phys. **C38** (1988) 371.
[13] C. DeMarzo *et al*, Phys. Rev. **D36** (1987) 8.
[14] J. Badier *et al.*, Z. Phys. **C31** (1986) 341.
[15] M. McLaughlin *et al.*, Phys. Rev. Lett. **51** (1983) 971.
[16] G. Bari *et al.*, Phys. Lett. **B163 (1985) 282.**
[17] A. C. Benvenuti *et al.*, Phys. Lett. **B189** (1987) 483.
[18] J. Ashmann *et al.*, Phys. Lett. **B202** (1988) 603.
[19] R. G. Arnold *et al.*, Phys. Rev. Lett. **52** (1984) 52.
[20] M. Luo, J. Qiu, and G. Sterman, Phys. Lett. **B279** (1992) 377.
[21] P. Aurenche, R. Baier, M. Montannaz, and D. SchiffNucl. Phys. **B297** (1988) 661.
[22] H. Baer, J. Ohnemus, and J.F. Owens, Phys. Rev. **D42** (1990) 61.
[23] M. J. Alguard *et al.*, Phys. Rev. Lett. **37** (1976) 1261.
[24] M. J. Alguard *et al.*, Phys. Rev. Lett. **41** (1978) 70.
[25] G. Braun *et al* Phys. Rev. Lett. **51** (1983) 1135.

[26] J. Ashman *et al* Phys. Lett. **264** (1988) 306.
[27] J. Ellis and R.L. Jaffe, Phys. Rev **D9** (1974) 1444.
[28] R. L. Jaffe and A. Manohar, Nucl. Phys. **B337** (1990) 509.
[29] D. Adams *et al* Phys. Lett. **B329** (1994) 399.
[30] A. V. Efremov and O.V. Teryaev, Sov.J.Nucl. Phys. **36**(1)(1982) 140.
[31] P. G. Ratcliffe, Nucl. Phys. **B264** (1986) 493.
[32] J. Qiu and G. Sterman, Phys. Rev. Lett. {67} (1991) 2264; Nucl. Phys. **B378** (1992) 52.
[33] X. Ji, Phys. Lett. **B289** (1992) 137.
[34] A. Schäfer, L Mankiewicz, P. Gornicki, and S. Güllenstern, Phys. Rev. **D47** (1993) R1.
[35] A. V. Efremov and O. V. Teryaev, private communication.
[36] D. L. Adams *et al.*, Phys. Lett. **B345** (1995) 569.
[37] D. P. Grosnick *et al.*, N. I. M. **A2900** (1990) 269.
[38] B. E. Bonner *et al.*, Phys. Rev. Lett. (1988) 1918.
[39] N. Akchurin *et al.*, Phys. Rev. **D 48** (1993) 3026.
[40] B. Margolis and G. H. Thomas, in AIP Conf. Proc. No. 42,High Energy Polarized Proton Beams, Ann Arbor, 1977, eds. A. D. Krish and A. J. Salthouse. (AIP, New York,1978) p. 173; G. Fäldt *et al.*, Nucl. Phys. **B41** (1972) 125.
[41] B. Z. Kopeliovich and L. I. Lapidus, Yad. FIz. **19** (1974) 218.[Sov. J. Nucl. Phys. **19** (1974) 114].
[42] A. V. Vasilevski *et al.*, "High Stability Strong Current Sources for HV Supply for Multichannel Cherenkov Total Absorption Spectrometer Counters", IHEP Preprint 84-2,Serpukov,1984.
[43] H.-U. Bengtsson and T. Sjöstrand, Computer Physics Commun. 46 (1987) 43, CERN-TH. 6488/92 and references therein.
[44] CERN Library Long Write-Up, W5013.
[45] G. Donaldson *et al.*, Phys. Lett. B73 (1978) 375.
[46] Particle Data Group, Phys. Rev. **D50** (1994) 1173-1826.
[47] R. Kephart *et al.*, Phys. Rev. **D11** (1976) 2909.
[47] A. M. Rossi *et al.*, Nucl. Phys **B84** (1975) 269.
[49] G. Donaldson *et al.*, Phys. Rev. Lett. **36 (1976) 1110.**
[50] F. W. Büsser *et al.*, Nucl. Phys. **B106** (1976) 1.
[51] J. F. Owens, Rev. Mod. Phys. **59**(1987) 465.
[52] D. W. Duke and J. F. Owens, Phys. Rev. **D30** (1984) 49.
[53] P. Aurenche and M. R. Whally, RAL-preprint, RAL-89-106.
[64] R. K. Ellis and J. C. Sexton, Nucl.Phys. **B269** (1986) 445.
[55] J. Botts *et al.*, Phys. Lett. **B304** (1993) 159.
[56] (NMC collaboration) P. Amoudruz *et al.*, Phys. Lett. **B295** (1992) 159-168.
[57] M. Glück, E. Reya, A. Vogt, Z. Phys. **C52** (1992) 127.
[58] P. Aurenche, R. Baier, M. Fontannaz, and D. Schiff, Nucl. Phys. **B286** (1987) 509.
[59] D. L. Adams *et al.*, IHEP-preprint IFVE-94-88,to be submitted to Phys. Rev. **D**.
[60] R. L. Jaffe and X. Ji, Nucl. Phys. **B375** (1992) 527.
[61] J. A. Bartelski, Phys. Rev. **D20** (1979) 1229.
[62] R. L. Jaffe, Comm. Nucl. Part. Phys. **14** (1990) 239.
[63] X. Ji, Phys. Rev. **D42** (1990) 3637.
[64] R. L. Jaffe and X. Ji, Phys. Rev. **D43** (1991) 724.
[65] J. Soffer and O. Teryaev, Phys. Rev. Lett. **71** (1993) 3609.
[66] J. Kodaira, Y. Yasui, and T. Uematsu Kyoto University preprint KUCP-71, Hiroshima University preprint HUPD-9411 (hep-ph/9408354).
[67] D. Adams *et al.*, Phys. Lett. **B336** (1994) 125.
[68] B. Ehrensperger, A. Schäfer, W. Greiner, and L. Mankiewicz, Phys. Lett. **B321** (1994) 121.
[69] N. Kroll and W. Wada, Phys. Rev **98** (1955) 1355.